Spatial Evolution of Small Wavelength Fluctuations in a Hall Thruster

Zachariah A. Brown* and Benjamin A. Jorns
University of Michigan

(Dated: September 28, 2019)

Abstract

The spatial evolution of small wavelength (< 1 cm) fluctuations in the Hall direction of a 9-kW class magnetically shielded Hall effect thruster is experimentally characterized. High-speed electrostatic probes are used to measure plasma density perturbations in the acceleration region and near field plume of this cross-field device. Two types of waves are observed: broadband turbulence in the low hundreds of kilohertz and megahertz oscillations characterized by distinct peaks in the measured power spectrum. The lower frequency content is shown to be commensurate with linear ion acoustic-like waves while the higher frequency oscillations are indicative of cyclotron resonances. It is found that the higher frequency content dominates the power spectrum in the upstream acceleration zone and saturates at a fraction (<0.002) of the thermal energy. Downstream of this region, the lower frequency content becomes dominant, growing until the total wave energy again saturates. It is proposed that both the upstream and downstream modes are the same oscillation, the electron drift instability, but in different limits. The transition from upstream to downstream dispersion may be explained by the electron drift instability undergoing an inverse energy cascade as it forms and propagates with the ion drift in the discharge.

* brownzac@umich.edu

I. INTRODUCTION

Hall effect thrusters are low-temperature, crossed-field plasma discharges that are commonly employed for electric propulsion. These cylindrical devices generate thrust by accelerating ions across an axial potential drop established between an upstream anode and a downstream cathode electron source. A magnetic field applied in the radial direction across the transverse electric field inhibits electrons from free streaming towards the anode but does not affect the motion of the ions. The presence of orthogonal magnetic and electric fields forces the electrons into an azimuthal $E \times B$ drift, the Hall effect drift, that increases electron residence time and allows for efficient ionization. Although Hall thrusters have an extensive space flight heritage, there are fundamental aspects of their operation that remain poorly understood. They are host to numerous instabilities, plasma oscillations,[1] and anomalous processes that influence their stability and performance[2]. One of the most critical but least understood processes is the existence of anomalous electron transport. In particular, the observed flux of electrons across magnetic field lines is orders of magnitude higher than could be explained by classical effects, e.g. particle collisions. To date, this poorly understood process has precluded the development of self-consistent models for these devices.

The need for both improved understanding and model fidelity of these devices has given rise to a number of efforts to investigate the source of anomalous electron transport. While many different mechanisms have been proposed to explain this effect [3–8], there is an emerging consensus in the community that the onset of micro-instabilities may be a dominant contributor[9]. Recent kinetic simulations [10–16] and analytical models [17–19] suggest that an electron drift instability (EDI) driven by the high $E \times B$ velocity of the electrons can significantly enhance electron mobility across magnetic field lines through particle-wave interactions. Guided by the these numerical results, Tsikata et al. showed, experimentally, the existence of EDI-like waves in a Hall thruster plasma[20, 21]. This seminal experiment, broadly representing a validation of theory, has helped establish the EDI as a leading contender to explain the anomalous transport.

Despite the growing body of correlational evidence pointing to the important role of the EDI for transport, there are a number of questions about the nature of this instability in the Hall thruster that have yet to be addressed experimentally. Perhaps the most pressing

is whether this wave actually exists in the so-called acceleration region of the thruster. This is a critical consideration since this zone, where the electric and magnetic fields are highest, is fundamental to the operation of Hall thrusters. It is where the majority of ion acceleration occurs. Understanding the mechanisms driving transport in this region is therefore paramount. With that said, although numerical simulations suggest that the EDI should be the dominant contributor to electron transport in this critical region, experimental measurements have not been able to access it—the results reported by Tsikata et al were performed downstream of this acceleration region where the electric and magnetic fields are weaker. As a result, it ultimately is not known if the EDI exists in the acceleration zone, or even if it does appear in this region, it is not clear that it would exhibit the same features (dispersion and energy content) as those reported for measurements performed downstream. This is a crucial consideration as the shape of the wave spectrum and its dispersion both mediate the interaction of the EDI with the electrons. Faced with this uncertainty about the EDI in the acceleration zone, there is a pressing need for experimental efforts to examine the plasma oscillations in the thruster and to document if and how the measured properties are connected to previous experimental and numerical work on this problem. To this end, the goal of this work is to characterize the spatial evolution of the plasma oscillations–their energy content and dispersion—as a function of position in a Hall effect thruster.

This paper is organized in the following way. In Section II. we review current models of the EDI and experimental evidence to date. In Section III. we provide a detailed summary of the methodology we employed to measure plasma oscillations. In Section IV. we present the results of the experimental study and in Section V. the measured waves are compared with the theories discussed in Section II. Lastly, we draw conclusions about the nature of the EDI in both the acceleration and downstream regions of Hall thrusters.

II. REVIEW OF THE $E \times B$ ELECTRON DRIFT INSTABILITY IN HALL EFFECT THRUSTERS

We show in Fig. 1 a schematic of a typical Hall thruster geometry along with the electric and magnetic fields. These devices accelerate ions via the electric field which is generated by applying a potential between an upstream anode and downstream cathode. While the potentials are set at the ends of the discharge channel, experiment and simulation have

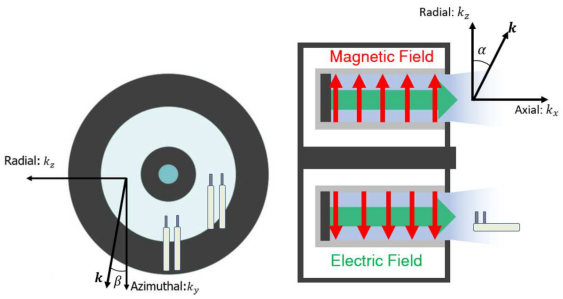

(a) (b)

FIG. 1: Schematic of Langmuir probes during interrogation of each wavevector component: a) Azimuthal and radial b) Axial.

shown that ions only accelerate across an extremely sharp potential drop slightly upstream of the location of the peak radial magnetic field strength, near the exit of the channel. This narrow "acceleration zone" is characterized by a strong local electric field that drives electrons into a high-speed, azimuthal Hall effect drift. These high-speed electrons traveling against relatively stationary ions can promote drift-driven instabilities—most notably the kinetic-based electrostatic instability known as the electron drift instability (EDI). The instability grows at the expense of the electron kinetic energy which acts as an effective drag on this species. This drag in turn can give rise to cross-field transport [19].

Following the analytical work of Ducrocq, Cavalier, and et al.[17, 18], the dispersion relation of the EDI in a Hall thruster geometry is given by

$$1 + k^2\lambda_{De}^2 + g\left(\frac{\omega - k_y V_d}{\omega_{ce}}, (k_x^2 + k_y^2)\rho^2, k_z^2\rho^2\right) - \frac{k^2\lambda_{De}^2\omega_{pi}^2}{(\omega - k_x v_p)^2} = 0, \tag{1}$$

where $g(\Omega, X, Y)$ is the Gordeev function defined as

$$g(\Omega, X, Y) = i\Omega \int_0^{+\infty} e^{-X[1-cos(\varphi)]-\frac{1}{2}\varphi^2+i\Omega\varphi} d\varphi. \tag{2}$$

Here ω is the oscillation frequency, ω_{ce} is the electron cyclotron frequency, ω_{pi} is the ion plasma frequency, $k = \sqrt{k_x^2 + k_y^2 + k_z^2}$ is the oscillation wavenumber, k_x is the wavevector component traveling in the axial direction, k_y is the component in the $E \times B$ direction, k_z is the component in the radial direction (along magnetic field lines), V_D is the azimuthal electron drift velocity, v_p is the ion beam velocity in the axial direction, λ_{De} is the Debye

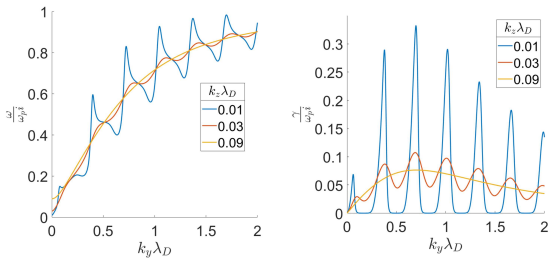

(a) (b)

FIG. 2: Solutions of the EDI dispersion relation, adapted from Cavalier et al[18] with different radial wave components (k_z). Frequency (a) and growth rate (b) are normalized by the ion plasma frequency (ω_{pi}) and wavenumber is normalized by the Debye length(λ_{De}).

length, and $\rho = V_{the}/\omega_{ce}$ is the electron Larmor radius at thermal velocity $V_{the} = \sqrt{T_e/M_e}$ where T_e is expressed in terms of energy. For plasma parameters typical of Hall thrusters, this dispersion yields oscillations with frequencies in the megahertz domain and resonant wavelengths on the order of millimeters or smaller; these occur at $k \approx m\omega_{ce}/V_d$ where m is the mode number.

Figure 2 shows dispersion relations for a typical Hall thruster plasma from Eqn. 1 where real frequency and growth rate are plotted versus azimuthal wavenumber. In the calculation of these solutions the radial wavenumber k_z is treated as a free variable. When we assume the wave does not propagate radially, $k_z \approx 0$, we see distinct resonances. As we allow for finite k_z, i.e. radial propagation, the discrete structure in both the real component of the dispersion and the growth rate transition into a continuous dispersion. Eventually, the resonance structure vanishes completely, and the dispersion collapses to an ion-acoustic wave:

$$\omega_R = \boldsymbol{k} \cdot \boldsymbol{v}_p \pm \frac{k c_s}{\sqrt{1 + k^2 \lambda_{De}^2}} \tag{3}$$

$$\gamma = \pm \sqrt{\frac{\pi M_e}{8 M_i}} \frac{\boldsymbol{k} \cdot \boldsymbol{v}_D}{(1 + k^2 \lambda_{De}^2)^{3/2}}, \tag{4}$$

where ω_R is the real frequency, γ is the growth rate, and c_s is the ion sound speed given by

$\sqrt{T_e/M_i}$. These equations yield a maximum growth rate for oscillations with a wavelength of $\lambda \approx 9\lambda_{De}$ and frequency of $\omega_R \approx \omega_{pi}/\sqrt{3}$.

A number of simulations on Hall discharges have resolved the EDI with dispersion in either the acoustic or cyclotron resonant form[10–12, 14, 22, 23]. Simulations and experiment diverge though in the nature–discrete or broadband–of the EDI. Indeed, as can be seen from the growth rates in Fig. 2, the dispersion has a wavelength associated with maximum growth— either at the resonances or the wavelength of maximum growth in the acoustic limit. This would suggest that any propagating mode would be dominated by this wavelength, thus appearing as a discrete structure. While the appearance of discrete, coherent waves has been borne out from simulation, to date, experimental results have shown instead a broadband structure without resonances or any dominant wavelength[20]. It should be noted, however, that most simulation results have focused on the acceleration region whereas the experimental works were performed (as outlined in Sec. I) downstream. There is a possibility then that the EDI may in fact exhibit a discrete structure experimentally in the acceleration region. Documenting this structure in this region, interpreting it in the context of the linear theory presented here, and understanding how it connects to the EDI downstream measurements are the driving goals for the experimental setup discussed in the next section.

III. EXPERIMENTAL SETUP

A. Facility and Thruster

For this experiment we employed the H9, a 9-kW class Hall effect thruster developed jointly by NASA's Jet Propulsion Laboratory, the University of Michigan, and the Air Force Research Laboratory [24, 25]. The H9 employs a magnetically shielded topography [26], and uses a center-mounted LaB_6 hollow cathode. This thruster was tested in the Large Vacuum Test Facility (LVTF) at the University of Michigan. In this campaign, LVTF employed 10 cryogenic pumps to reach a base pressure of 5×10^{-7} Torr-Xe and a working pressure of 7×10^{-6} Torr-Xe as recorded by a Stabil Ion gauge located approximately 1 meter adjacent to the thruster exit plane following industry standards [27]. The H9 was operated at 300V and 15A with a xenon flow rate of 163 sccm through the anode and a 7% cathode flow

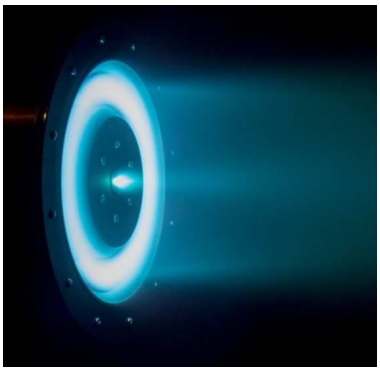

(a)

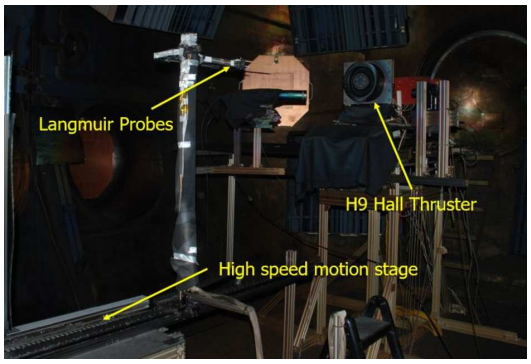

(b)

FIG. 3: a) H9 Hall effect thruster and b) Experimental setup in the Large Vacuum Test Facility at the University of Michigan. Diagnostics and motion stages are highlighted.

fraction. The thruster body was electrically tied to the cathode.

B. Wave probes

We employed a set of translating cylindrical Langmuir probes biased to ion saturation current to characterize the plasma oscillations in the plume of the H9 thruster. A bias voltage of -36V was applied with batteries to place the probe well below the typical floating voltages observed in Hall thrusters[28]. In principle, the current collected on these probes thus is proportional to the ion density, $i_{sat} \propto n_i$. In this work, we exploit this fact and follow

Ref. [29] to relate measured fluctuations in the ion saturation current to plasma density fluctuations: $\tilde{i}/\bar{i} \approx \tilde{n}/\overline{n}$ where we use the general convention that $\tilde{x}$ denotes perturbations about a mean value of $\overline{x}$. This approximation is based on the thin-sheath approximation and that the electron temperature does not change substantially on the time-scale of the high-speed fluctuations we are measuring. The constant temperature assumption is only a weak requirement, however, since as shown in Ref. [30], even large changes in electron temperature only marginally perturb the relationship between density and ion saturation current. On the other hand, the assumptions about the thin-sheath can be violated. We note that for the the ratio of our probe radius to the Debye length (10-15 throughout the plume), there are regions where the ion collected current is in the so-called transitional sheath domain[31]. However, in applying the more complete expressions for ion saturation introduced in Ref. [31], we found this only led to an error of less than 15% compared to the thin sheath approximation. For the remainder of this work, we therefore assume $\tilde{i}/\bar{i} \approx \tilde{n}/\overline{n}$ valid to within $\sim$15%.

The probes consisted of 0.38 mm radius tungsten rods with an exposed length of 3.8 mm. The length and radius were chosen to provide a sufficiently large probe area to resolve less than 0.01% fluctuations in relative density with our data acquisition system while also maintaining an aspect ratio of at least 1:10 to ensure a cylindrical sheath. The resulting radius is also small compared to the width of the discharge channel which can help reduce perturbations to the plasma as the probes are inserted into the plume[32]. This length, however, limited the spatial resolution of our measurements as the ion saturation current was collected over the length of the probe. The positions reported in this work thus are referenced with respect to the center of the probe body. As we discuss further in Sec. III., we injected multiple, spatially-separated probes into the plasma and measured correlations in their signals to infer the dispersion of the fluctuations in ion saturation density. We employed two probes in three orientations for this purpose (see Fig.1) to measure the axial, radial, and azimuthal components of the oscillations. In each case, the tips were separated by 4.7 mm allowing direct measurement of wavenumbers between -688 and 688 rad/m. This separation (several Debye lengths) was dictated by the need to prevent the sheaths from the probes from overlapping.

C. Probe translation

In order to provide spatially-resolved measurements, we implemented a high-speed injection technique to insert probes into the thruster discharge. Following Refs. [33–35], this high-speed reciprocating sampling helped limit probe damage that can result from prolonged exposure to the energetic near-field plasma and minimize perturbations to the plasma. The probes were mounted on a linear induction motion stage (Fig. 3) that translated from the exit plane of the thruster at 50 cm/s with the ion saturation current signal recording continuously at 100MS/s. For our study, we injected these probes along the thruster channel centerline from a location of $z/L = 1$ to $z/L = 3$ where L denotes the length of the channel and z is the distance from the anode.

Refs. [33–35] have shown that active probing can perturb thruster plumes. In order to assess whether the probes were impacting the plasma in this experiment, we monitored two key global properties of the discharge, the DC current and its oscillations, as the probes were inserted. The power spectrum of the discharge current did not change with respect to the position of the probes unless they were injected past the exit plane and into the discharge channel. For all results presented in this work we restricted our measurement domain only to the region downstream of the exit plane. We note, however, that as discussed in Jorns et al.[34], global metrics do not necessarily indicate that the plasma is undisturbed. It should be kept in mind that it is possible that the plasma in our configuration still was impacted by the probe insertion.

With that said, in addition to the high-speed injection method, we also collected wave fluctuation data at fixed positions between 0.5-1 channel lengths downstream of the exit plane. Here the probes were far enough from the thruster that they were able to sample data for longer periods without damage. These fixed position measurements yielded an order of magnitude more samples at a particular position than the high-speed method and thus provided higher spectral resolution. As we will discuss in Section IV. B, these probes focused on lower frequency oscillations and were sampled at 10MS/s. We also note here that while the fixed downstream probes collected wave information in all three directions, we only were able to generate data on the azimuthal wave component for measurements near the acceleration zone.

IV. RESULTS

A. Spatially-resolved power spectra

We show in Fig. 4a an example of the raw ion saturation current collected by one of wave probes as it was injected along thruster centerline. The decrease in magnitude with normalized distance from the exit plane is an indication of the drop in density as the plume is expelled from the thruster. The properties of interest to us in this study, however, are the small-scale fluctuations that occur on top of this curve. In order to analyze these properties and relate them to spatially-resolved measurements of the wave properties, we employed the following analysis. First, we binned the data from each probe by axial location (shown notionally as vertical lines in Fig. 4a) into sixteen segments. We then subdivided the data in each bin into 200 sequential time segments and divided the signal by the time-averaged density in each sample ($\tilde{i}_{sat}/\overline{i}_{sat}$). Per our discussion from the previous section, this yielded an estimate of ($\tilde{n}_i/\overline{n}_i$). An example of one of these 200 time series from a spatial bin is shown in Fig. 4b. We next applied a Fourier analysis on each of the 200 time-varying signals in the spatial bin and averaged to yield a power spectrum of the average spectral content of the fluctuations at each spatial location. Figure 5 shows a sample result of this analysis, plotting the power spectrum intensity as a function of frequency and position in the plume where the distance from the anode (z) has been normalized by the length of discharge chamber (L).

As can be seen from Figure 5, the dominant feature consists of well-defined fluctuation bands in the MHz domain that are spaced approximately 3MHz apart up to 20MHz. Upstream of the peak magnetic field, denoted by the dashed black line at $z/L = 1.3$, the spectral content of the lower frequency harmonics is at its weakest and approximately constant as a function of position. Half a channel length downstream of the exit plane, the relative amplitudes of the megahertz fluctuations spike before decaying downstream and oscillations spanning the 100-500 kHz domain develop. The magnitude and spacing of these frequencies, which are below the local ion plasma frequency, is qualitatively consistent with the linear dispersion of the EDI introduced in Sec. II. This spectral content therefore is the central focus of this investigation. As an aside, we note that this plot also shows that there is spectral content in the vicinity of 45MHz before and after the location of peak magnetic field strength ($z/L = 1.3$), but this frequency is well above the ion plasma frequency which

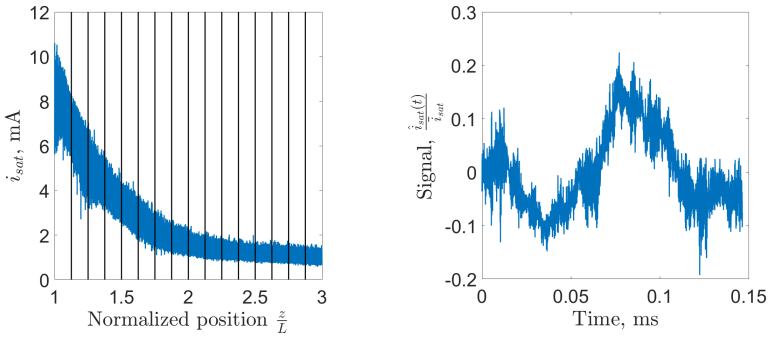

(a) (b)

FIG. 4: a) Ion saturation current as function of position during probe injection. An example of the spatial binning (vertical lines) used to generate spatially-resolved dispersion relations is shown. b) The relative density perturbations as function of time in one of the 200 time samples of a spatial bin.

is considered the maximum for EDI oscillations. We therefore do not consider it further for this investigation. With that said, we do note that these oscillations occur in a similar frequency and wavenumber domain to previous high-frequency measurements of Lazurenko et al[36].

Due to the low spectral resolution of Figure 5, it is difficult to see unambiguously how the oscillations are changing at low (<1 MHz) frequencies. In order to better resolve the spatial evolution of spectral content in this region, we repeated our analysis with only four spatial bins. This yielded a finer frequency resolution of 1.4kHz. The resulting power spectrum in each bin is shown in Figure 6 where we have marked the resonances with red vertical lines. We now can see more clearly that the growth of low frequency broadband oscillations coincides with a decrease in power of the megahertz oscillations. We have also included for reference the power spectrum of the discharge current during probe injection in Figure 6. As discussed in Section III.C, the discharge current spectrum did not appreciably change in amplitude or spectral content during probe injection. Additionally, this result also illustrates that besides the breathing-mode oscillations at 10kHz, we do not observe the same high-frequency spectral content in the discharge current. This suggests that the wave probes are

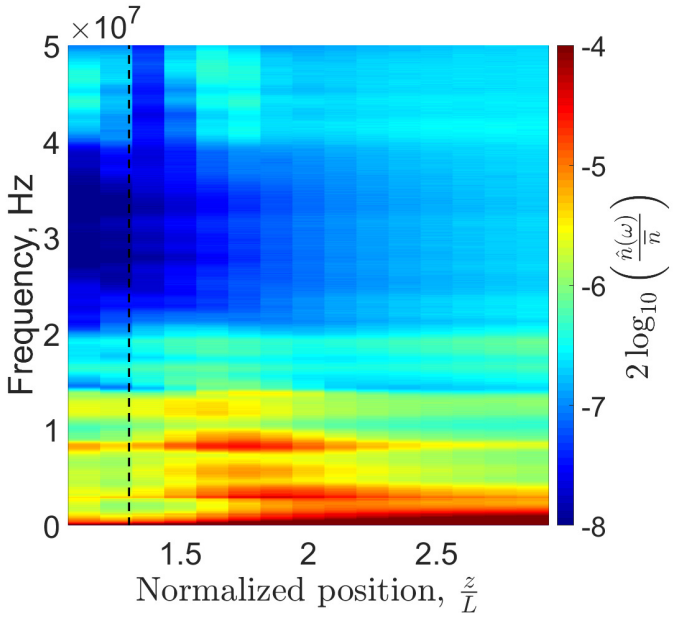

FIG. 5: Power spectrum as a function of normalized position along channel centerline of the Hall thruster. Distance from the anode z is normalized by the discharge chamber length L. The location of the peak magnetic field at $z/L = 1.3$ is indicated by a dashed black line.

measuring plasma-borne modes. Lastly, although we see an evident sharp peak at 1 MHz in all of the results, this likely was electrical noise in the measurement circuit. Its unnormalized amplitude remained constant at all positions in the plume and was present even when the thruster was off.

While we reserve a full discussion of the implications of these findings for Section V., we note that these initial measurements already suggest that the EDI has a fundamentally different character in the acceleration region of the thruster as compared to the downstream. Indeed, we see in Fig. 6 that our measured spectrum downstream of $z/L = 1.5$ is dominated by a broadband, incoherent content between 100-500 kHz in agreement with previous experimental results that showed a broadband spectrum downstream. Moving upstream, where presumably the instability initially first grows due to the strong Hall drift in this region, we

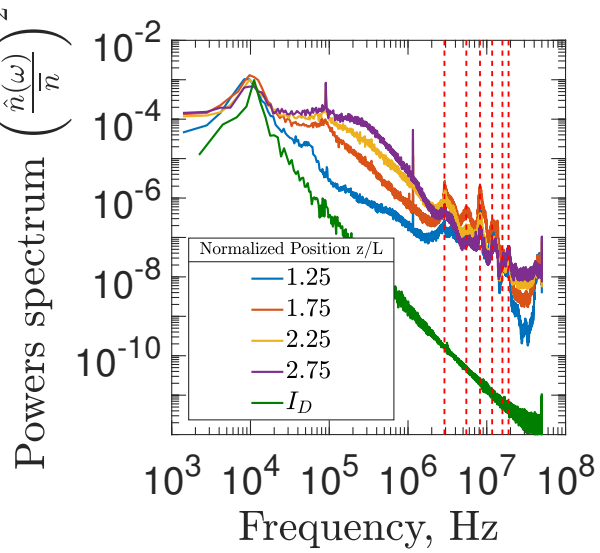

FIG. 6: Power spectra along channel centerline using only 4 spatial bins. Megahertz peaks are highlighted with dashed red lines. The discharge current power spectrum is also shown for reference.

see that in fact the resonant structures in the megahertz domain become more dominant. This is consistent with initial linear growth and is in line with the simulation results that have been reported to date in 2D reduced dimensional kinetic models. Our results show an evident transition between these two states as function of position in the plume.

B. Spatially-resolved dispersion

Expanding on the conclusions from the previous section, we can apply additional analysis to the spatially-resolved ion saturation probe data to look for evidence of wave dispersion. This methodology is based on examining the correlation between ion saturation probe signals from a combination of two probes as they are inserted in the plasma. In particular, following Ref. [29], if we know the separation between these probes, we can use Fourier analysis to determine if there is a wavenumber, k, along the line defined by the probes associated with

oscillation frequency, ω:

$$k(\omega) = \frac{1}{\Delta x} \tan^{-1} \left[\frac{\mathrm{Im}(\mathcal{F}[i_{sat1}(t)]\mathcal{F}^*[i_{sat2}(t)])}{\mathrm{Re}(\mathcal{F}[i_{sat1}(t)]\mathcal{F}^*[i_{sat2}(t)])} \right], \tag{5}$$

where Δx is the distance between the probes, $\mathcal{F}, \mathcal{F}^*$ denotes the Fourier transform and its complex conjugate, and $i_{sat:1,2}$ is the ion saturation current from adjacent probes 1 and 2. Following the approach of Beall et al.[37], we apply a histogram analysis to the same spatial and time bins from Figure 4 to generate intensity plots of frequency versus wavenumber at each spatial location. An example result taken from spatial location z/L = 1.5 is shown in Figure 7a with a frequency resolution of 22kHz and a wavenumber resolution of 27 rad/m^{-1}. The result in Figure 7a shows evident structure in the dispersion plots which are correlated with the well-defined resonances in the megahertz frequency range we noted in Figure 6. Indeed, at each band the wave is spread out across the wavenumber domain and in many cases appears to exhibit aliasing, i.e. phase wrapping on the k-axis. Aliasing in this context stems from the fact that probe sets have a maximum measurable wavenumber dictated by the distance between the tips. Oscillations with wavenumbers larger than the maximum value set by the probe spacing are aliased by the cross-correlation technique to smaller wavenumbers. For example, if a probe can measure wavenumbers between -600 and 600 rad/m then plasma oscillations with a wavenumber of 750 rad/m would be measured as having a wavenumber of -450. This would suggest that the observed oscillations have dispersion, i.e. propagate, but the wavelengths are too small to resolve with our finite probe spacing. While aliasing in this context likely precludes us from making definitive comments on the dispersion (i.e. it is difficult to resolve any evident patterns), we return to a discussion of this in section IV. B in which we show that the short wavelength EDI (Eqn. 1) could have a dispersion similar to the one we observe here.

We show in Fig. 7b dispersion relations at a location (z/L = 2) further downstream of the discharge exit. In this case, as expected from the power spectrum observations, the intensity plot is dominated by content at lower frequency. These plots with 22kHz frequency resolution do not have sufficient detail to resolve nuances in the dispersion structure, resulting only in an evident peak at the bottom of the Beall plot around $k = 200$ rad/m^{-1}. However, by using data from our fixed probes (mounted downstream) with higher spectral resolutions, we can appropriately resolve the dispersion features in this region. The Beall plots from this data are shown in Figure 8 for each wave direction: azimuthal, axial, and radial, and

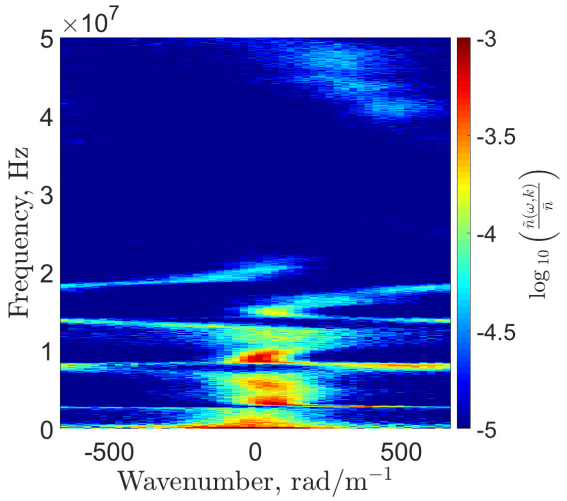

(a)

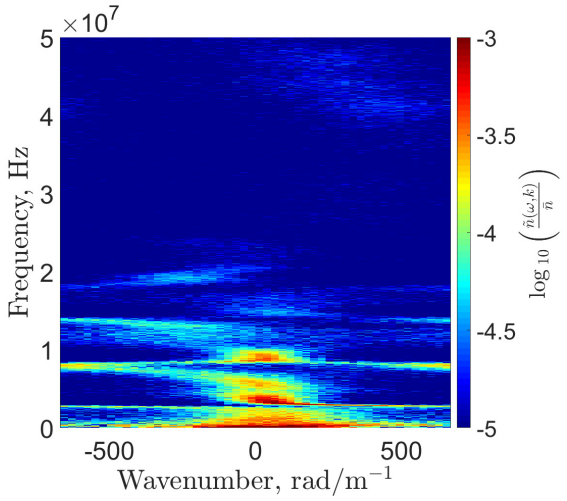

(b)

FIG. 7: Beall plot for the azimuthal direction at (a) 1.5 L and (b) 2.0 L downstream of the anode and at channel centerline. The frequency resolution is 22kHz and the wavenumber resolution is 27 rad/m.

show a linear dispersion in 50-500kHz domain. Although, this linear dispersion does not appear in the Beall plots until after z/L = 1.5, and upstream of this location there is no visible dispersion in this frequency range. This linear behavior is consistent with the results of Tsikata et al. who reported a linear dispersion downstream[20, 21], though we note that our maximum resolve-able wavenumber is an order of magnitude lower than the ranges they reported. Physically, this result lends further support to the notion that the fundamental structure of the propagating oscillations changes with position, transitioning from the complex dispersion at higher frequency and small wavelength (Fig. 7a) to this more acoustic-like result downstream (Fig. 8a).

We can further quantify aspects of this acoustic-like dispersion by fitting lines to the intensity plots and multiplying the resulting slope by 2π to determine the wave speed. This yielded a phase velocity in each direction of 4, 10, and 50 km/s for the azimuthal, axial, and radial components respectively. This result suggests that the acoustic wave propagates primarily in the azimuthal direction but is tilted into the axial direction (α) by 20 degrees and into the radial direction (β) by -5 degrees; where negative wavenumbers denote propagation opposite the basis vector(see Figure 1). Functionally, this suggests that in addition to azimuthal propagation, the modes are also directed axially away from the thruster and radially inward. This stands in contrast to the work of Tsikata et al. [21] who measured that the modes propagate axially inward. The reason for this discrepancy is not known, though we note that physically, the fact that these acoustic modes in our measurements are directed away from the thruster is consistent with the notion that these oscillations are carried by the ions. In addition, the phase velocity in the azimuthal direction is commensurate with the ion sound speed which qualitatively is consistent with the EDI in the acoustic limit (Eqn. 3). This lends further support to the supposition that the modes have transitioned in this region to the acoustic limit. Finally, we note that we observe nonlinear behavior in the axial dispersion where the phase velocity increases at frequencies higher than 300kHz. The explanation for this behavior in the context of the linear dispersion theory outlined in Sec. II is not evident, though this departure from linearity dispersion may not be surprising given the simplifying assumptions underlying this derivation (weak gradients and a Cartesian geometry). Physically, however, we note that this nonlinear behavior, which is characterized by a non-changing value of wavenumber in the axial direction above a certain frequency, suggests the propagating modes at frequencies above 300 kHz turn to be more in

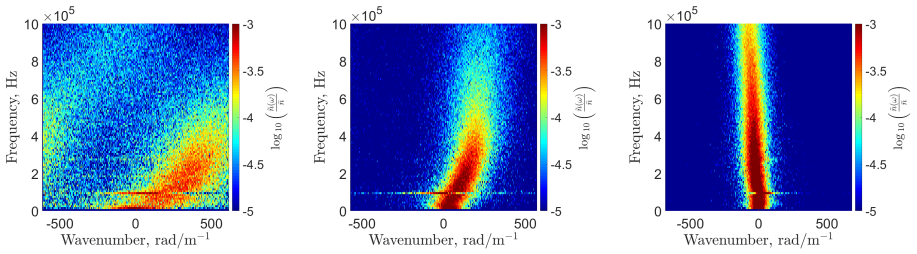

(a) (b) (c)

FIG. 8: Beall intensity plots at z/L = 2 downstream of the thruster anode for each wavevector component: a) azimuthal, b) axial, c) radial. The frequency resolution is 5 kHz and the wavenumber resolution is 9 rad/m

the azimuthal direction.

V. DISCUSSION

In light of the results presented in the previous section, we now can turn to the governing questions for this work: does the EDI exist in the acceleration zone, are its properties fundamentally different than EDI measurements downstream, and ultimately, how are the waves measured in these two zones connected? To this end, in the following section we begin by comparing the measured modes in the acceleration zone to the linear dispersion and then discuss the transition of the wave in the context of nonlinear transport across lengthscales.

A. Comparison of measured dispersion and theory

In section IV. we showed the presence of two distinct oscillations: high-frequency resonant-like waves dominant near the exit plane and low frequency ion acoustic-like oscillations dominant further downstream. While we were able to demonstrate that the low-frequency content is comparable to the measured acoustic-like waves that have been reported in previous work, the nature of the high frequency modes at the exit plane is less evident. As discussed previously, while the frequencies are the right order of magnitude expected of EDI harmonics, the true wavenumber of our measured waves is likely obscured

TABLE I: Assumed plasma parameters for solution of EDI dispersion

$n_0 \times 10^{17}$ m^{-3}	T_e, eV	ω_{ce}, MHz	v_p, km/s	β, deg	$k_z\lambda_{de}$	V_d, km/s
6 - 12	20 - 40	257	16	20	0.005	$V_{the}/2$

by aliasing effects and prevents a definitive comparison to the EDI. It is also important to acknowledge the possibility that these modes may be nonphysical–a result of probe induced effects. To this latter point, we recall that in monitoring the global metric for thruster operation, the discharge current, we found that the probe insertion did not change the oscillating character of the thruster. Moreover, this higher frequency content did not appear at any point in the discharge current power spectrum. This suggests that the measured waves are in fact a plasma borne mode. Even allowing for this fact, however, there is also the possibility that this plasma mode may be a response to the probe presence, e.g. an effect of sheath-induced oscillations. This does not seem consistent with the measurements since qualitatively we anticipate that such sheath-related oscillations should appear on the time scale of sheath formation, i.e. the plasma frequency, whereas our measured frequencies were below this limit. With that said, however, we cannot categorically dismiss the possibility that these measured waves are probe-induced as we did not have an independent, non-perturbative mechanism to assess them. As we discuss in the following though, the mode number and dispersion content, if we attempt to correct for the aliasing, are physically consistent with the linear dispersion of the EDI.

To this end, we would expect that the short wavelengths of the EDI mode in this frequency range could not be measured directly with our setup. We thus cannot make a direct comparison or validation against the theoretical description outlined in Section II. As an alternative, by using the known EDI dispersion relation(Eqn. 1) with physically-informed assumptions about the local plasma parameters, we can calculate the expected harmonic frequencies of the EDI. Since we are able to measure these unambiguously we can compare the predictions to our measured results. If the numerically solved resonance frequencies closely match our measured values, we could take this as correlative evidence that high frequency oscillations are attributable to the EDI.

We elect to do this comparison between theory and experiment at conditions representative of the acceleration region. This is driven primarily by the theory that this is the region

where the linear growth is expected to be highest (i.e. where the Hall drift, the driving source for the instability, is highest). We calculated the theoretical resonance frequencies at this location following the method used by Cavalier et al.[18] by solving Eqn. 1. There are several free plasma parameters in this equation that could affect the calculation of the resonant frequencies, but many can be estimated with reasonable assumptions based on previous Hall thruster measurements[38, 39]. We consider a range of densities and electron temperatures that could manifest in the acceleration region(Table I), but fix all other quantities, except for the electron drift velocity V_d. The dispersion relation is extremely sensitive to the electron drift velocity and we adjusted this parameter until a best fit was achieved at about half the electron thermal speed which is of the order seen in simulations.[14, 40]. Finally, as mentioned in Sec III. we were unable to measure the radial wavenumber, so for the theoretical dispersion we set the radial wavenumber (k_z) low enough to maintain distinct resonances. We used a value of $k_z\lambda_{De} = 0.005$, but the exact value was not important for this analysis as long as the resonances were still intact. This is borne out by Figure 2, which shows that the value of the real frequency at the resonances remains unchanged with radial wavenumber.

The predicted EDI resonances from the analytical dispersion along with the measured resonant frequencies are presented in Figure 9. The error bars on the experimental data correspond to the full width half max of each resonance peak in the power spectrum(see Figure. 6), while the error bars for the numerical solution represent the range of possible results for the values listed in Table. I. The markers for the numerical solution show the overall best fit for $n_0 = 6.5 \times 10^{17}$ m^{-1} and $T_e = 25$ eV. There is close agreement between experimental and numerical values across the 8 measured resonances with the numerical solution slightly over-predicting the frequency for the first few modes and slightly under-predicting at the highest modes. With that said, the close agreement across 8 mode numbers for a wide range of densities and temperatures and with an electron drift velocity closely matching values from simulations provides strong correlational evidence that the measured megahertz oscillations are EDI cyclotron resonances.

Despite this agreement between theory and experiment in the acceleration zone, there is one notable feature in the measured modes not anticipated by the linear theory: the invariance of the frequency values of the resonances. Indeed, the background plasma properties (most significantly the electron cyclotron frequency) vary as a function of spatial position,

which would suggest from Eqn. 1 that in turn the resonant frequencies also should vary. This is not reflected in our measurements where the resonant frequencies remain relatively constant. While we do not have sufficient data to conclusively identify why this occurs—in particular we cannot see if the wavelength of the oscillation changes through the plume instead—there is a possible explanation from the measurements and underlying theory. Linear saturation should occur quickly in the acceleration region, and it is possible that further downstream, where the linear growth rate is significantly diminished by the lower electric field and $E \times B$ drift velocity, the wave no longer has the energy to grow at different resonant frequencies. This assumes that the original resonant frequencies still satisfy the real component of the dispersion relation in the far-field. While our measurements are insufficient to determine the dispersion relation at every point in the plume we note that parameters typical of the far-field region ($T_e = 3$ eV, $n_0 = 1 \times 10^{17}$ m^{-3}, $v_p = 20$ km/s, $V_D = 50$ km/s, and $\omega_{ce} = 209$ MHz) yield a dispersion relation with a significantly reduced growth rate (Fig.10a) and a real frequency very close to the original resonances (Fig.10b).

With these caveats in mind, we ultimately conclude that at least correlationally, the measured modes in the acceleration zone appear to be EDI. Though, they exist with fundamentally different properties than the acoustic like EDI oscillations measured downstream. Indeed, the measured resonant-like waves actually seem to be more in line with the predictions of linear growth. This result physically is intuitive given that this region, i.e. the region of maximum Hall drift, is likely where the modes originate in the thruster.

B. Quantifying transition from acceleration zone to downstream region

The previous two sections have shown that the observed waves appear to be consistent with the EDI either in both the resonant and the acoustic-like limit depending on where the measurement is made. The structure exhibits discrete wavelengths in the upstream region and broadband oscillations downstream. The former, as discussed above is consistent with the predictions of linear dispersion theory: the EDI power spectrum should be dominated by discrete frequencies corresponding to cyclotron resonances. The latter state with its broadband character, however, is not intuitive and does not directly follow from linear theory. Indeed, even allowing for the case of finite k_z which we showed in Sec. II can eliminate the cyclotron resonances, the linear growth still has a maximum coincident with

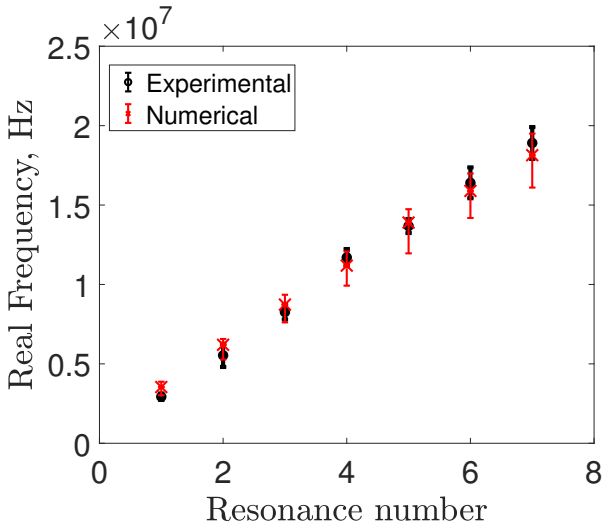

FIG. 9: Comparison between experimentally measured resonance frequencies and numerical solutions for values typical of the acceleration zone (Table. I)

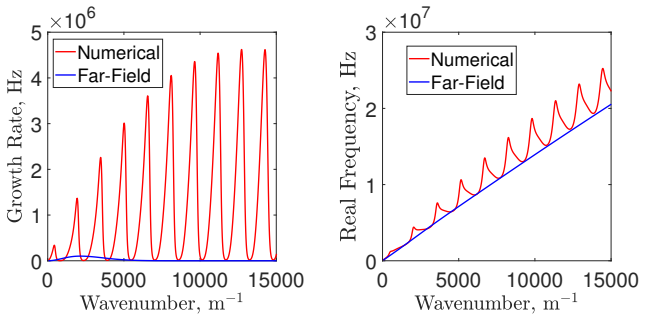

FIG. 10: a) Growth rate and b) frequency for analytical solutions of the EDI dispersion relation. The red curves are the best-fit solution for the parameters typical of the acceleration zone ($n_0 = 6.5 \times 10^{17}$ m^{-1} and $T_e = 25$ eV) while the blue curves use values typical of the far-field plume: $T_e = 3$ eV, $n_0 = 1 \times 10^{17}$ m^{-3}, $v_p = 20$ km/s, $V_D = 50$ km/s, and $W_{ce} = 2e8$ Hz, otherwise using the same parameters from Table I.

the ion plasma frequency. We do not see such a peak in the measured dispersion. With this in mind, we next turn to the question as to if and how the EDI in the acceleration zone is connected to this downstream state.

To this end, the hypothesis we propose here is informed by the work of Janhunen et al[11, 12]. The downstream state is the nonlinear result of an inverse energy cascade from cyclotron resonances toward the lowest mode numbers and then into a long wavelength oscillation much larger than the fundamental resonance wavelength. Physically, in this process, two high frequency resonances "beat" against one another and couple energy between the resonances and the beat frequency of the two waves. This process effectively transfers energy to lower frequencies and thus larger lengthscales. For example, the m = 3 and m = 5 modes would beat together and transfer energy to the m = 2 mode. This wave-wave coupling process ultimately gives rise to a power law like decay in frequency spectrum. This hypothesis is supported by the many similarities between our measured power spectra as function of position (Figure 5) and the numerical results of Janhunen (Figure 14 in reference [12]) where the authors show the power spectrum as function of wavenumber vs time. Both show clear resonances at high wavenumber/frequency that gradually decay verses time/position as a low wavenumber/frequency oscillation appears. Since the simulation of Janhunen did not model the axial direction we interpret the temporal evolution of the EDI seen in 2D as equivalent to the spatial changes seen in our experiment as the instability evolves while being carried downstream by the beam plasma. This is supported by both the characteristic transient time of the beam plasma traveling from the acceleration region to where we observe the broadband low frequency oscillations and the time scale of the energy cascade seen in the simulation being on the order of μs.

We can expand on this interpretation quantitatively by examining the spatial evolution of the normalized wave-energy density, (W/n_0T_e). For electrostatic waves, this can be approximated as[41]

$$\frac{W}{n_0T_e} = \sum_{\omega} \left(\frac{\phi(\omega)}{T_e}\right)^2, \tag{6}$$

where the summation is taken over the frequency domain corresponding to the wave of interest and $\phi(\omega)$ is the amplitude of plasma potential fluctuations. Physically, this represents the relative magnitude of energy in the oscillation range compared to the thermal background and is a measure of the relative strength of the oscillations. In order to relate this

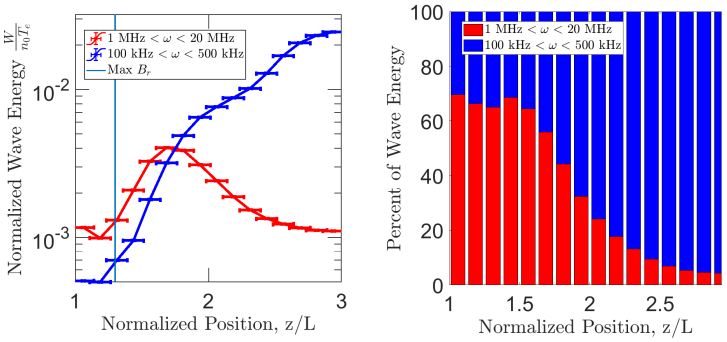

(a) (b)

FIG. 11: The normalized wave energy density (a) and relative strength of modes(b) at various points in the plume of the H9 along channel centerline are shown relative to the location of peak magnetic field, denoted by the light blue vertical bar at z/L = 1.3. Frequencies between 1 and 20 MHz are from the resonances and frequencies between 100 and 500 kHz are due to the broadband acoustic oscillations.

quantity to the parameters we measured, we note that the plasma density fluctuations for the electrostatic EDI waves can be related approximately as potential fluctuations by the Boltzmann response, $\tilde{n}/\overline{n} \approx \tilde{\phi}/T_e$. This allows us to write the normalized wave energy density exclusively as a function of our measured property $\tilde{n}/\overline{n}$ and eliminates the requirement of concurrent temperature and density measurements.

Armed with this definition, we show in Fig. 11a the normalized wave energy as a function of position along channel centerline for both classes of oscillations that we have documented: the low frequency broadband (100-500kHz) and the resonances (1-20MHz). The first notable feature is that the wave energy density is a finite fraction (0.002) of the thermal energy density within the acceleration region. This suggests that the mode may have reached a saturated state, i.e. the wave growth is limited. This type of saturation is not unexpected in this region which is characterized by the strongest $E \times B$ drift. Indeed, reduced dimension numerical simulations have shown that when the electron drift is strong (i.e. a substantial fraction of the Mach speed), wave growth can be capped by effects such as ion wave trapping [19]. Downstream of the acceleration zone, we see that the energy in the spectrum undergoes

a change coinciding with growth of the low frequency turbulence. In particular, upstream of the peak magnetic field (z/L = 1.3), where we anticipate the EDI will first onset due to the strong E × B drift, we see that the resonances are the primary source of wave energy. Immediately downstream of the peak magnetic field, both the low and high frequency modes grow together in strength until the high frequency waves reach a maximum at about z/L = 1.6. After this location two transitions occur. First, the low frequency broadband oscillations overtake the cyclotron resonances in terms of relative strength. This is indicated in Fig. 11b where the relative amplitude of the two oscillations are plotted with position. Second, as discussed in Sec. IV. this location is where the linear dispersion becomes visible in the Beall plots. After this point, the resonances decay in strength while the broadband oscillations continue to grow until z/L = 3. Although, as shown in Fig. 6 the first and third resonances are still visible downstream. These two figures thus show quantitatively the evident interplay in energy between the oscillations described in our hypothesis.

With that said, one interesting caveat to our interpretation is that we see that the resonant structure persists (Fig. 6) even when the broadband oscillations dominate. On the other hand, in previous experimental work, Tsikata et al did not record any resonances even though they were measuring in the same frequency range. The work by Janhunen may offer a resolution. Our probes measure fluctuations in ion density while Thomson scattering instead measures electron fluctuations. According to this previous numerical work, the nonlinear cascade towards long wavelength is significantly stronger for electrons compared to the ions. While the ion oscillations retained their resonant modes at the end of the simulation, in the electrons the presence of all but the first mode had disappeared. Therefore, Thomson scattering measurements downstream of the acceleration region would lead to different observations than electrostatic probing, potentially without resonances.

From a practical perspective, if this inverse cascade is a real mechanism, our results have implications for the understanding and approach to modeling of the micro-turbulence that contributes to anomalous cross-field electron transport in Hall effect thrusters. Indeed, as the growth and saturation of the EDI appears to be a highly nonlinear process, it can be inferred that its interaction with the electrons (and thus its drag-inducing effect) similarly must be nonlinear. Any model capable of predicting the transport in a real thruster geometry must consider this effect, either modeling it explicitly with a full kinetic approach or developing closures for fluid approximations that reflect the inverse energy cascade across

lengthscales. In particular, it is prudent that all future kinetic simulations must use grids that are sufficiently large to resolve our observed long wavelength oscillations.

In summary, the measured results correlationally support the hypothesis we have proposed. Within the acceleration region, the EDI develops with a linear growth, which results in discrete cyclotron resonances. As the instability propagates downstream, its properties are dominated by nonlinear effects that ultimately lead to broadband long wavelength oscillations. Thus, in addition to showing in the previous section that EDI likely exists in the acceleration zone, we have a plausible explanation for why and how the shape of the EDI power spectrum is causally connected to downstream measurements.

VI. CONCLUSION

In this paper, we have presented the results of an investigation of the electron drift instability in a Hall thruster's near field plume and acceleration region. In light of previous experimental work that has been performed in studying this mode, the driving considerations for our study were trying to determine if the EDI actually exists in the thruster acceleration zone and how this EDI evolves as a function of position in the thruster. We have found that in the acceleration region, the EDI does exist and is characterized by cyclotron resonances in the 1-20 MHz domain. This is consistent with the predictions from linear growth theory. In the downstream region, on the other hand, the power spectrum exhibits a fundamentally different character. The resonances still persist but the dominant feature is that the power spectrum is characterized by a broadband turbulent shape exhibiting an power law-like decay. While we have shown that both types of waves can be consistent with EDI waves– one in the discrete cyclotron resonance region and one in the acoustic limit–we have also sought to propose an explanation for how the two might be linked. To this end, we have proposed an explanation informed by previous numerical work[11, 12], which suggests that the downstream measurements are an evolved nonlinear state of the EDI which onsets in the upstream, acceleration zone. The resonances develop following linear growth in the acceleration zone and could undergo an inverse energy cascade in the downstream region that gives rise to the linear acoustic waves. We have plotted the evolution of the energy associated with the resonances and broadband turbulence to show correlationally that this type of interplay of energy across lengthscales may in fact occur. We theorize that this

cascade, which is enhanced for electrons compared to ions, is responsible for the absence of resonances observed in Thomson scattering measurements reported in previous studies[20].

In the context of the central question for Hall thrusters about the role of instabilities in driving cross-field transport, this work ultimately offers new insight into the role of the EDI in these thrusters. The observation of its transition from linear growth to a turbulent state suggests that the growth of this mode and interaction with the plasma are ultimately a nuanced and complex process. Indeed, these nonlinear effects ultimately will need to be considered self-consistently for efforts to relate the EDI to the steady-state electron dynamics in these systems.

ACKNOWLEDGMENTS

Work supported by National Science Foundation Graduate Research Fellowship Program Grant No DGE 1256260. Any opinions, findings, and conclusions or recommendations expressed in this material are those of the author(s) and do not necessarily reflect the views of the National Science Foundation.

[1] E. Y. Choueiri, Physics of Plasmas **8**, 1411 (2001).

[2] J. P. Boeuf, Physics of Plasmas **121**, 011101 (2017).

[3] N. B. Meezan, W. A. Hargus, and M. A. Cappelli, Physics Review E **62**, 026410 (2001).

[4] C. Boniface, L. Garrigues, G. J. M. Hagelaar, J. P. Boeuf, D. Gawron, and S. Mazouffre, Applied Physics Letters **89**, 161503 (2006).

[5] S. Barral, K. Makowski, Z. Peradzyński, N. Gascon, and M. Dudeck, Physics of Plasmas **10**, 4137 (2003).

[6] N. Gascon, M. Dudeck, and S. Barral, Physics of Plasmas **10**, 4123 (2003).

[7] M. S. McDonald and A. D. Gallimore, in *32nd International Electric Propulsion Conference* (2011).

[8] C. L. Ellison, Y. Raitses, and N. J. Fisch, Physics of Plasmas **11**, 013503 (2012).

[9] J. P. Boeuf and A. Smolyakov, Physics of Plasmas **25**, 061001 (2018).

[10] T. Lafleur, S. D. Baalrud, and P. Chabert, Physics of Plasmas **23**, 053502 (2016).

[11] S. Janhunen, A. Smolyakov, O. Chapurin, D. Sydorenko, I. Kaganovich, and Y. Raitses, Physics of Plasmas **25**, 011608 (2018).

[12] S. Janhunen, A. Sydorenko, D. Sydorenko, M. Jimenez, I. Kaganovich, and Y. Raitses, Physics of Plasmas **25**, 082308 (2018).

[13] A. L. Ortega, I. Katz, and V. H. Chaplin, in *35th International Electric Propulsion Conference* (2017).

[14] J. P. Boeuf and L. Garrigues, Physics of Plasmas **25**, 061204 (2018).

[15] A. Héron and J. C. Adam, Physics of Plasmas **20**, 082313 (2013).

[16] I. Katz, V. H. Chaplin, and A. L. Ortega, in *2018 Joint Propulsion Conference, AIAA Propulsion and Energy Forum* (2018).

[17] A. Ducrocq, J. C. Adam, and A. Heron, Physics of Plasmas **13** (2006).

[18] J. Cavalier, G. Lemonie, N amd Bonhomme, S. Tsikata, C. Honore, and D. Gresillon, Physics of Plasmas **20**, 082108 (2013).

[19] T. Lafleur, S. D. Baalrud, and P. Chabert, Physics of Plasmas **23**, 053503 (2016).

[20] S. Tsikata, N. Lemoine, V. Pisarev, and D. M. Gresillon, Physics of Plasmas **16**, 033506 (2009).

[21] S. Tsikata, C. Honore, N. Lemoine, and D. M. Gresillon, Physics of Plasmas **17**, 112110 (2010).

[22] J. C. Adam, A. Heron, and G. Laval, Physics of Plasmas **11**, 295 (2004).

[23] T. Lafleur and P. Chabert, Plasma Sources Sci. Technol. **27**, 015003 (2017).

[24] R. R. Hofer, S. E. Cusson, and R. B. Lobbia, in *35th International Electric Propulsion Conference* (2017).

[25] S. E. Cusson, R. R. Hofer, R. B. Lobbia, B. A. Jorns, and A. Gallimore, in *35th International Electric Propulsion Conference* (2017).

[26] I. G. Mikellides, I. Katz, R. Hofer, and D. Goebel, Applied Physics Letters **102**, 023509 (2013).

[27] J. W. Dankanich, M. Walker, M. W. Swiatek, and J. T. Yim, Journal of Propulsion and Power **33**, 668 (2017).

[28] J. M. Haas, *Low-perturbation interrogation of the internal and near-field plasma structure of a Hall thruster using a high-speed probe positioning system*, Ph.D. thesis, University of Michigan (2001).

[29] B. A. Jorns, I. G. Mikellides, and D. M. Goebel, Phys. Rev. E **90**, 063106 (2014).

[30] B. Nold, T. T. Ribeiro, Ramisch, Z. Huang, H. W. Müller, B. D. Scott, and U. Stroth, New Journal of Physics **14**, 063022 (2012).

[31] R. B. Lobbia and B. E. Beal, Journal of Propulsion and Power **33**, 566 (2017).

[32] N. Sternberg and V. Godyak, Physics of Plasmas **24**, 093504 (2017).

[33] J. Haas, G. G. Spanjers, J. McFall, and R. A. Spores, in *Proceedings of the 34th AIAA/ASME/SAE/ASEE Joint Propulsion Conference and Exhibit* (1998).

[34] B. A. Jorns, D. M. Goebel, and R. R. Hofer, in *51st AIAA/SAE/ASEE Joint Propulsion Conference* (2015).

[35] L. Grimaud, A. Pétin, J. Vaudolon, and S. Mazouffre, Review of Scientific Instruments **87**, 043506 (2016).

[36] A. Lazurenko, G. Coduti, S. Mazouffre, and G. Bonhomem, Physics of Plasmas **15**, 034502 (2008).

[37] J. M. Beall, Y. C. Kim, and E. J. Powers, Physics of Plasmas **53**, 3933 (1982).

[38] I. G. Mikelliedes, I. Katz, R. R. Hofer, and D. M. Goebel, in *48th AIAA/ASME/SAE/ASEE Joint Propulsion Conference and Exhibit* (2012).

[39] E. T. Dale and B. A. Jorns, Physics of Plasmas **26**, 013516 (2019).

[40] T. Lafleur, P. Chabert, and A. Bourdon, Physics of Plasmas **25**, 061202 (2018).

[41] R. Z. Sagdeev and A. A. Galeev, *Nonlinear Plasma Theory* (New York: Benjamin, 1969).

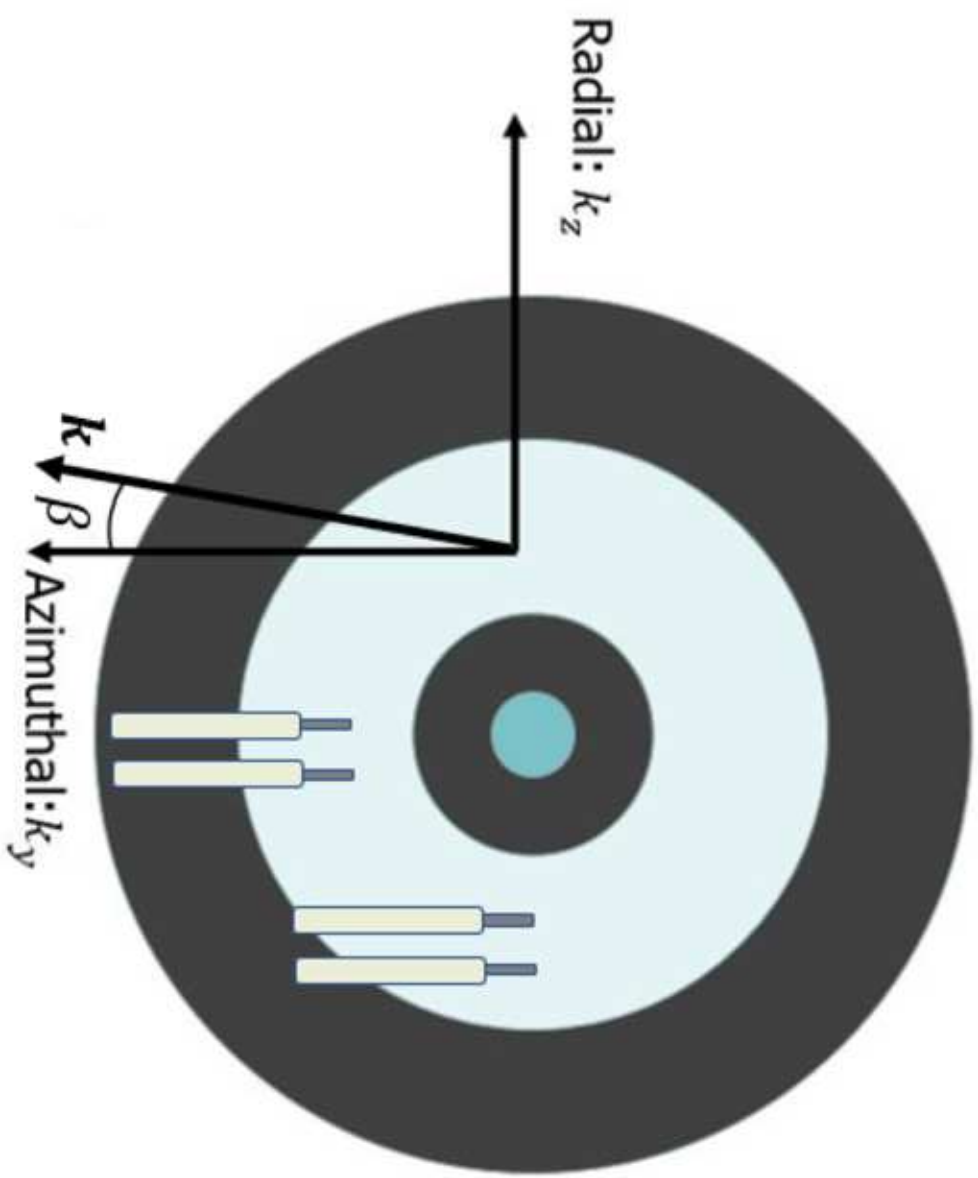

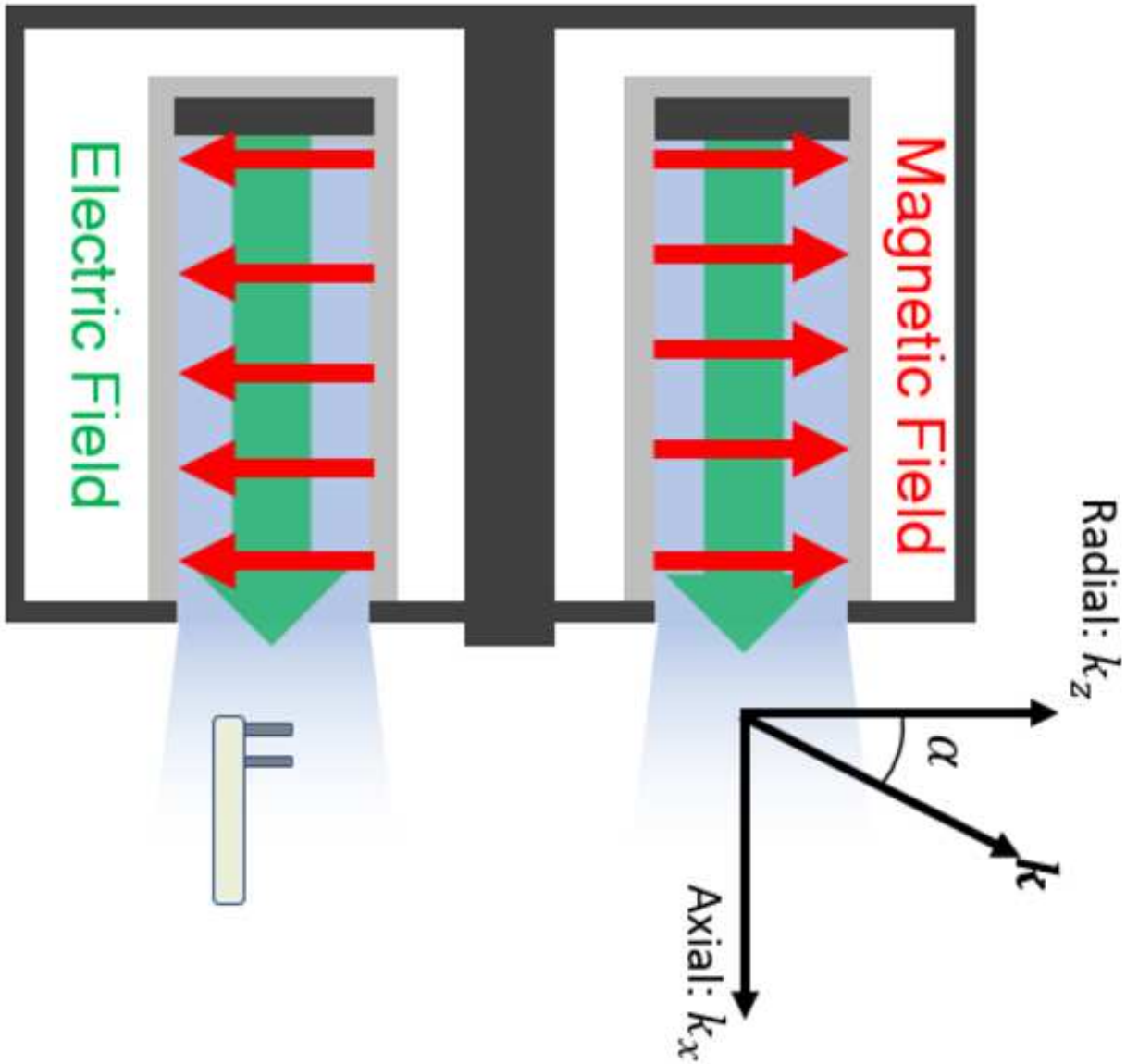

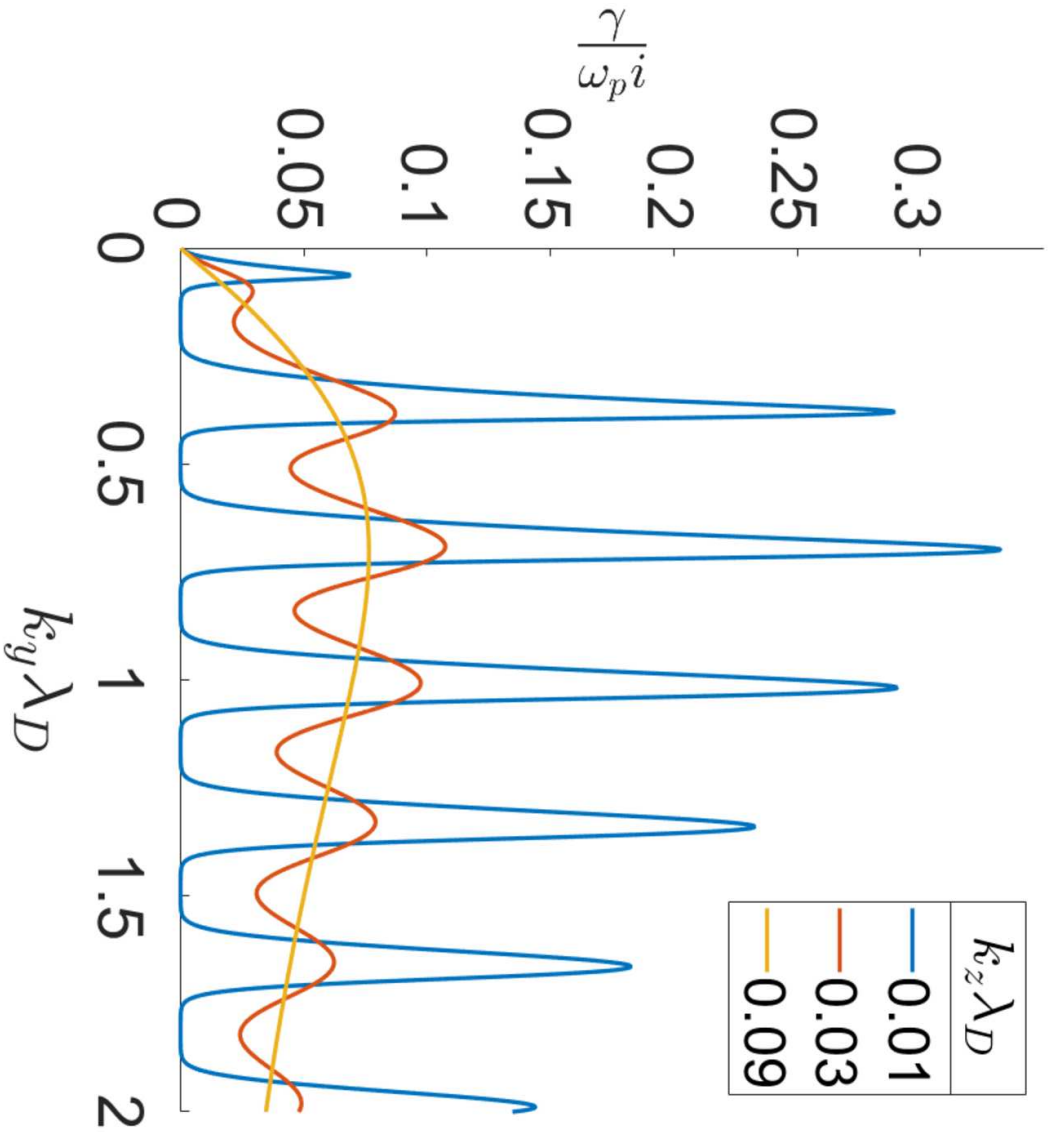

PLEASE CITE THIS ARTICLE AS DOI: 10.1063/1.5116708

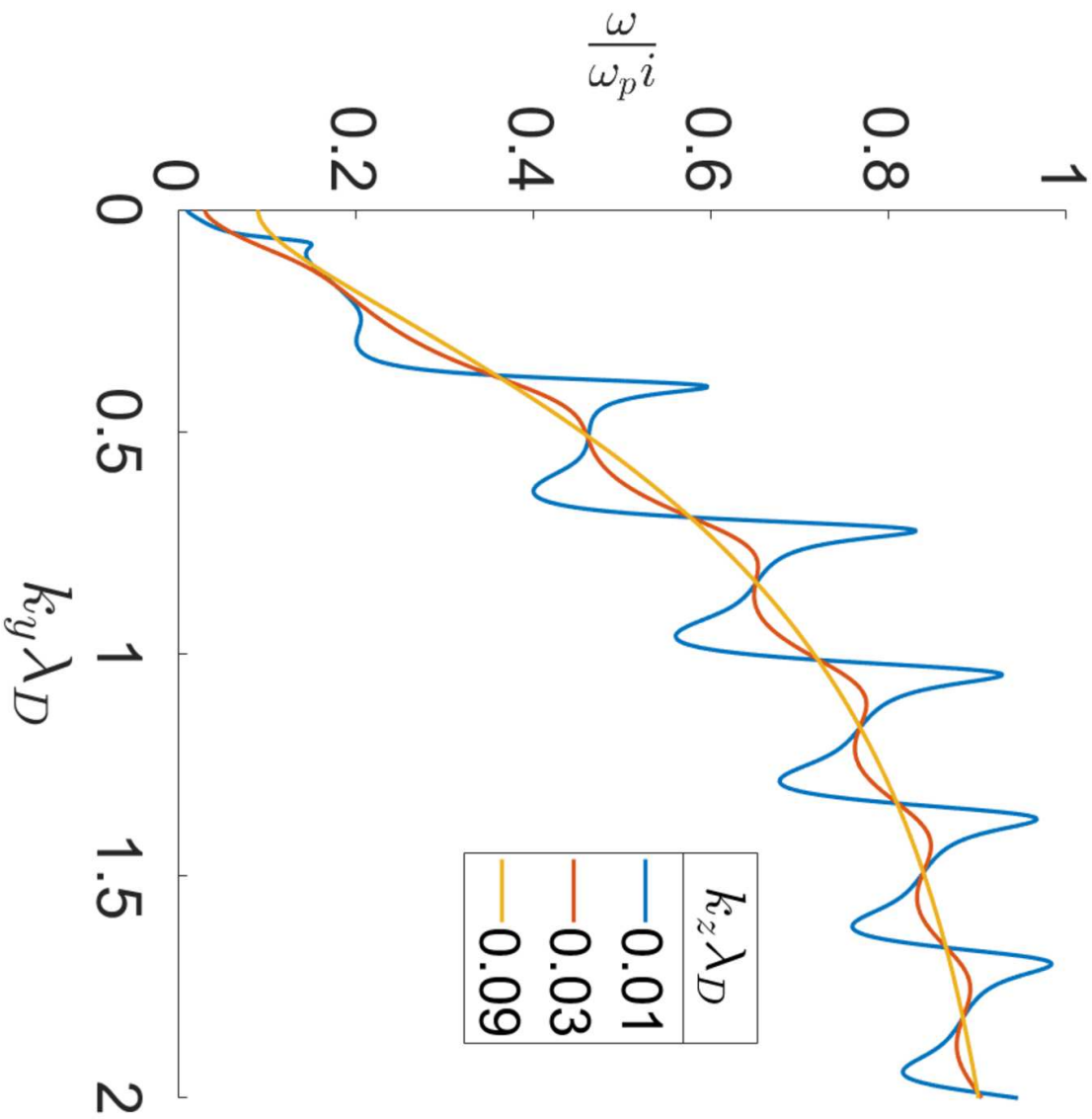

PLEASE CITE THIS ARTICLE AS DOI: 10.1063/1.5116708

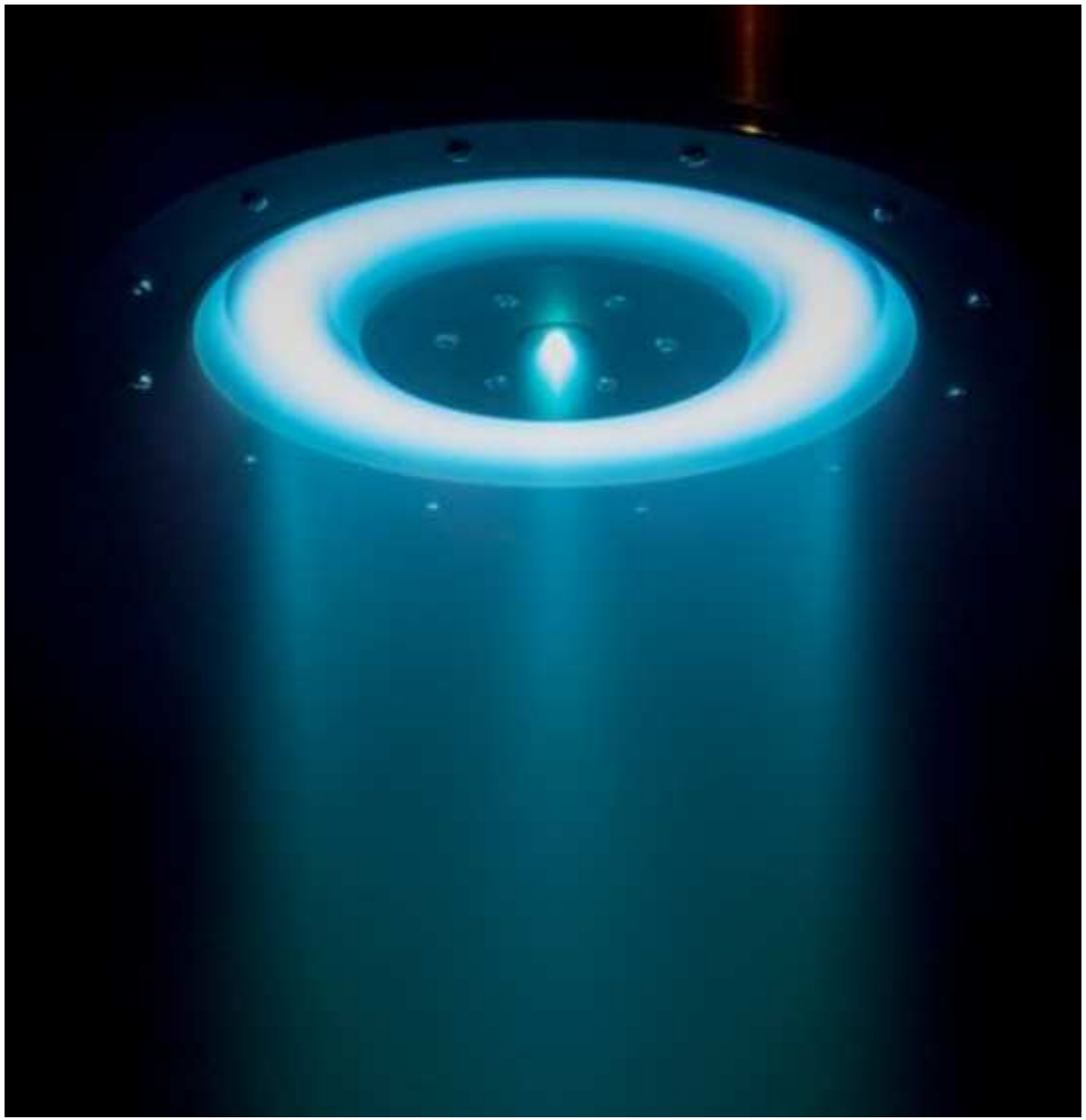

PLEASE CITE THIS ARTICLE AS DOI: 10.1063/1.5116708

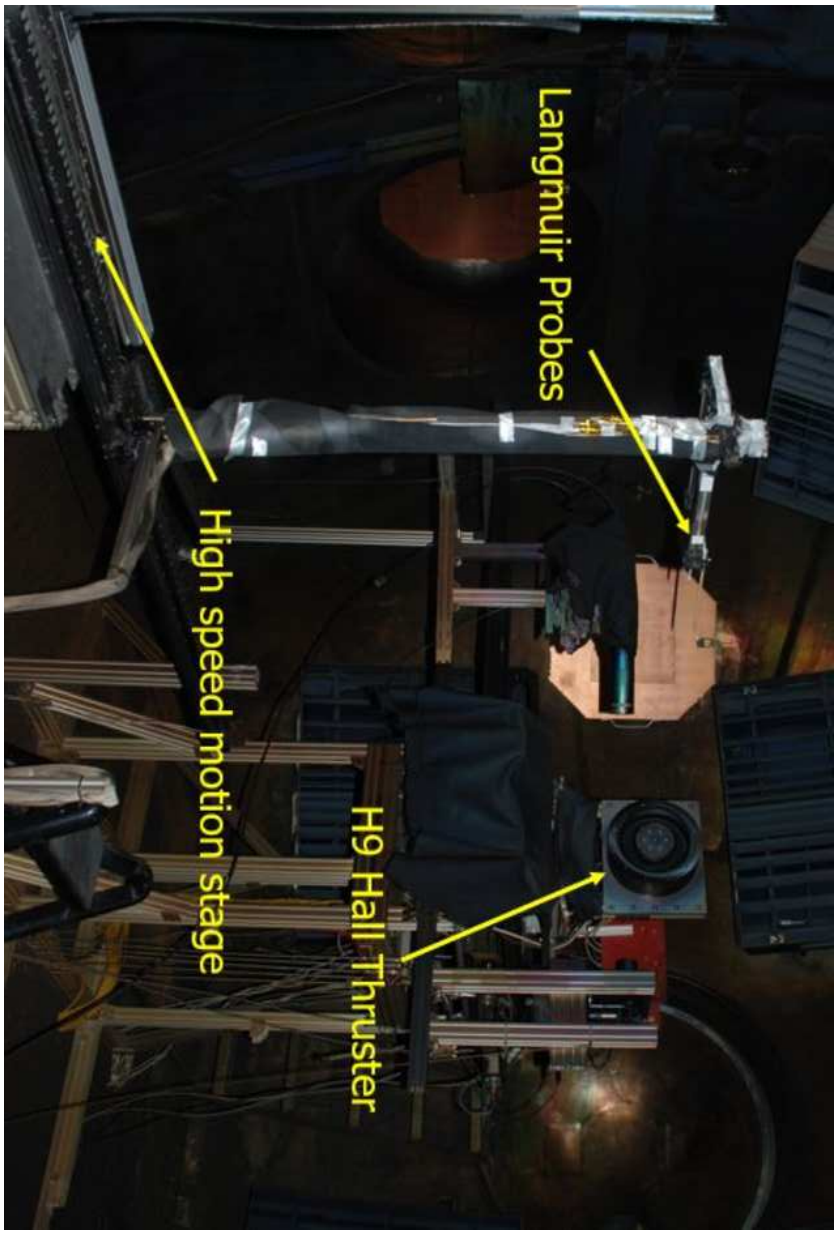

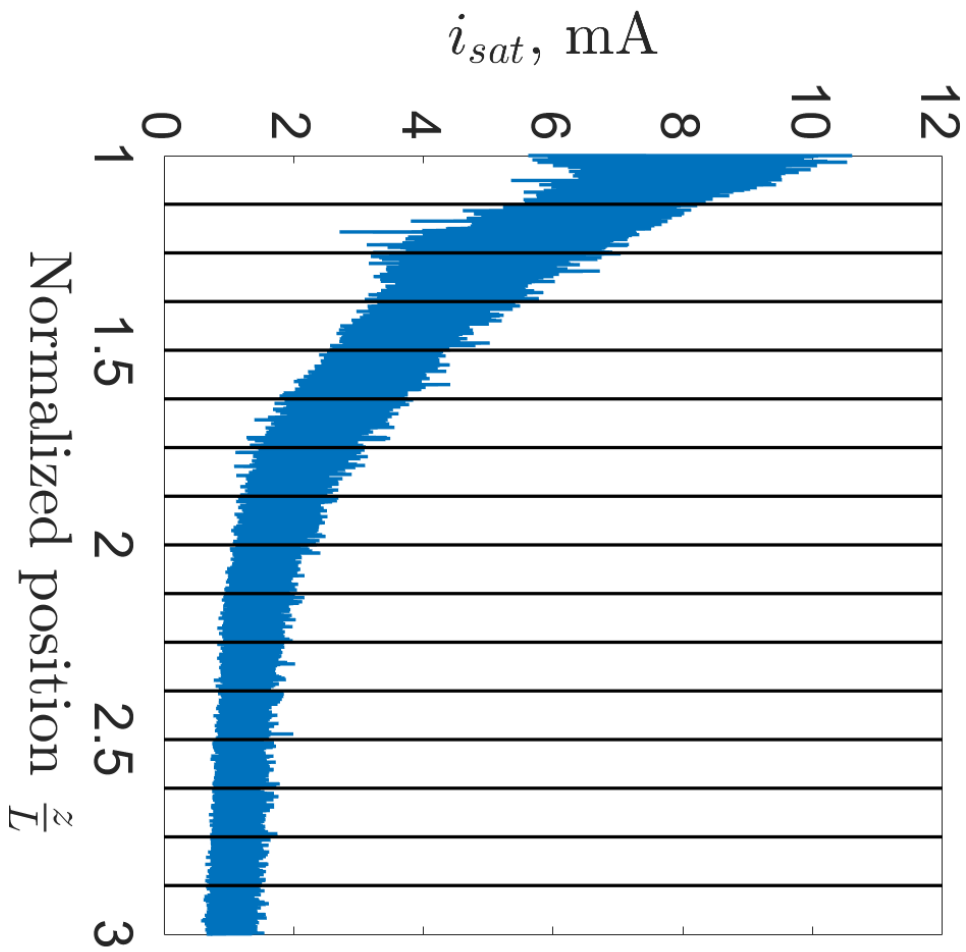

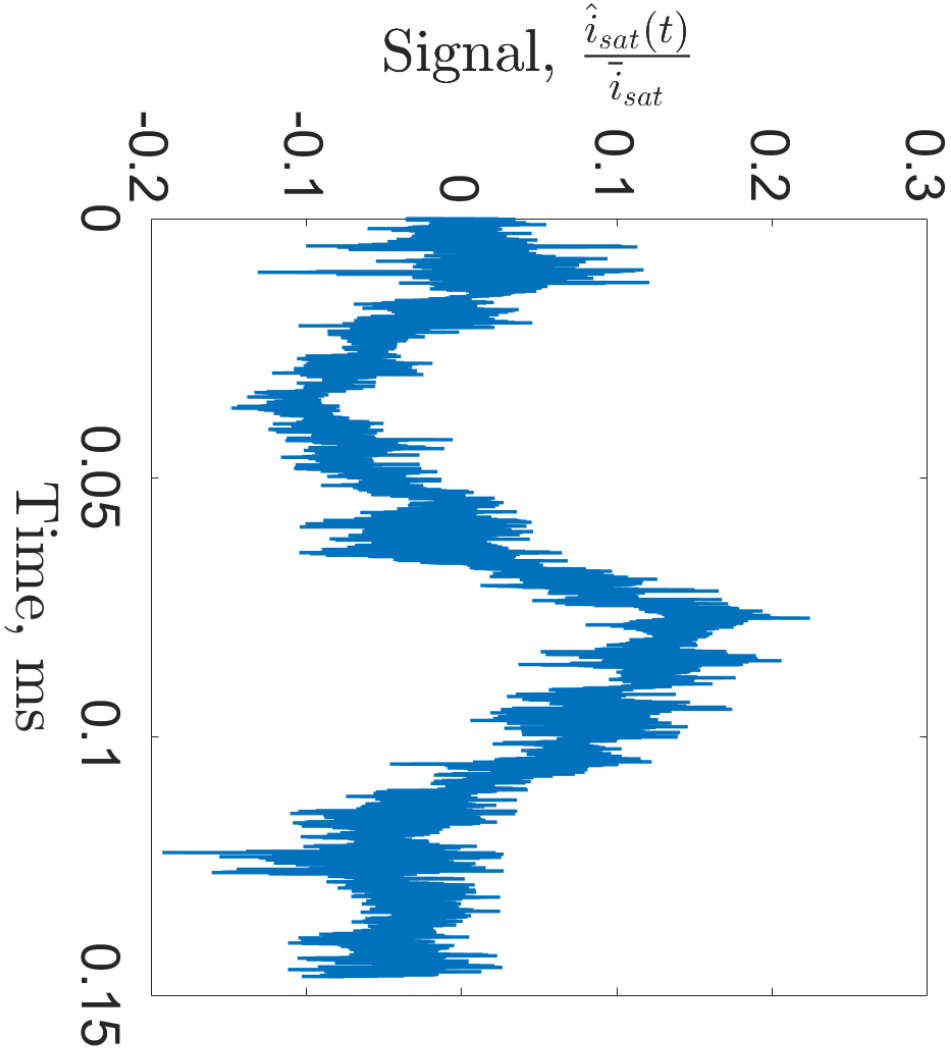

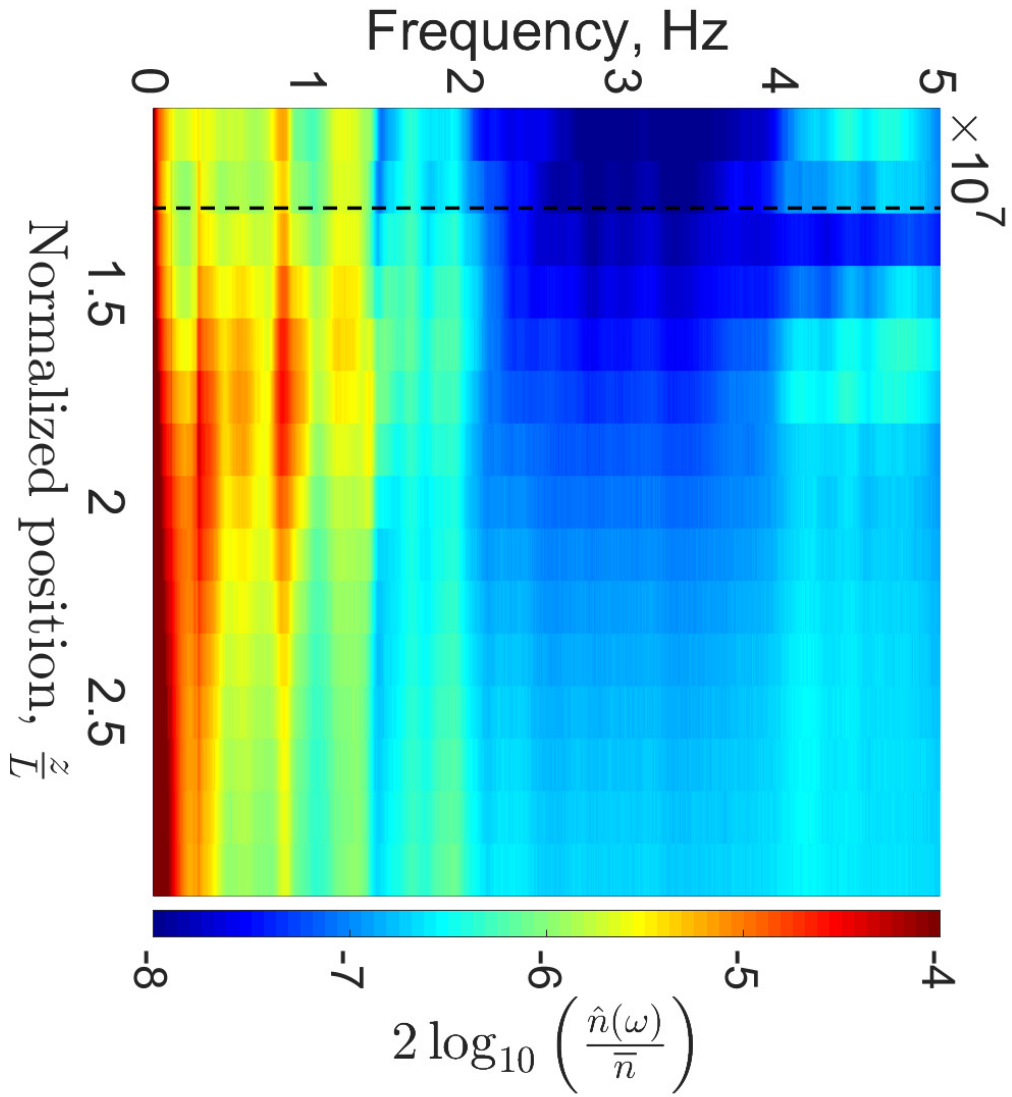

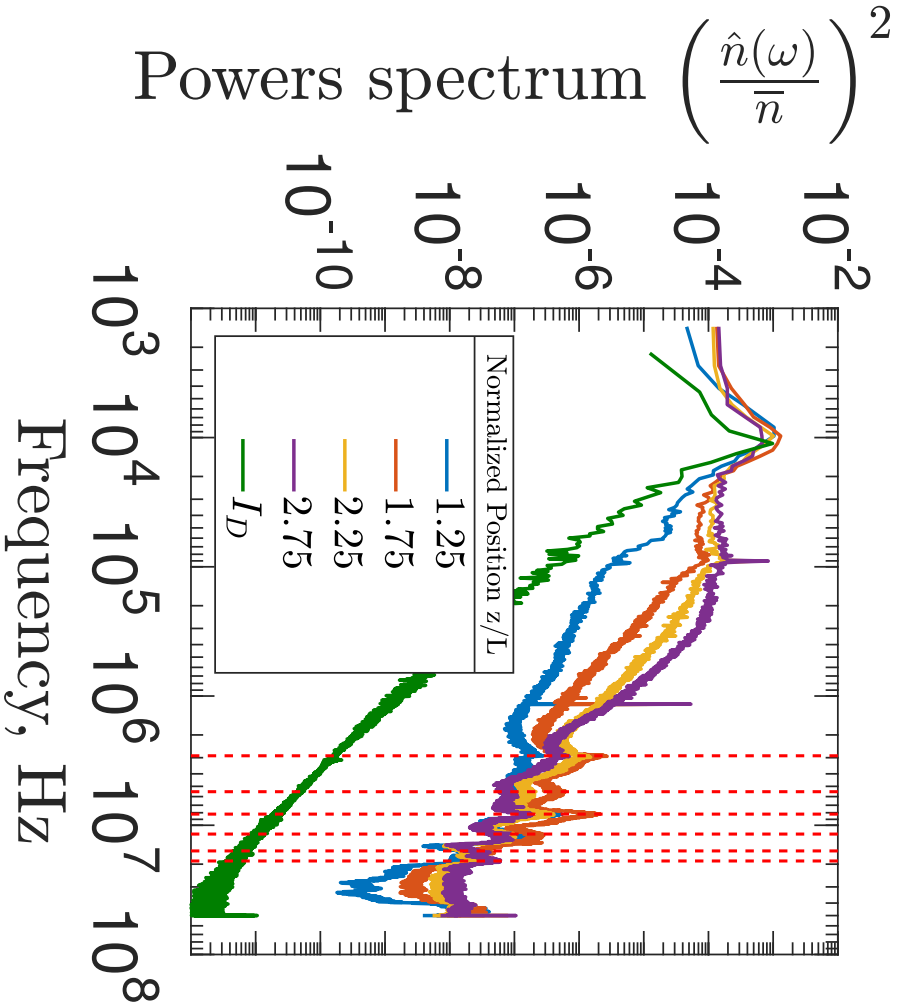

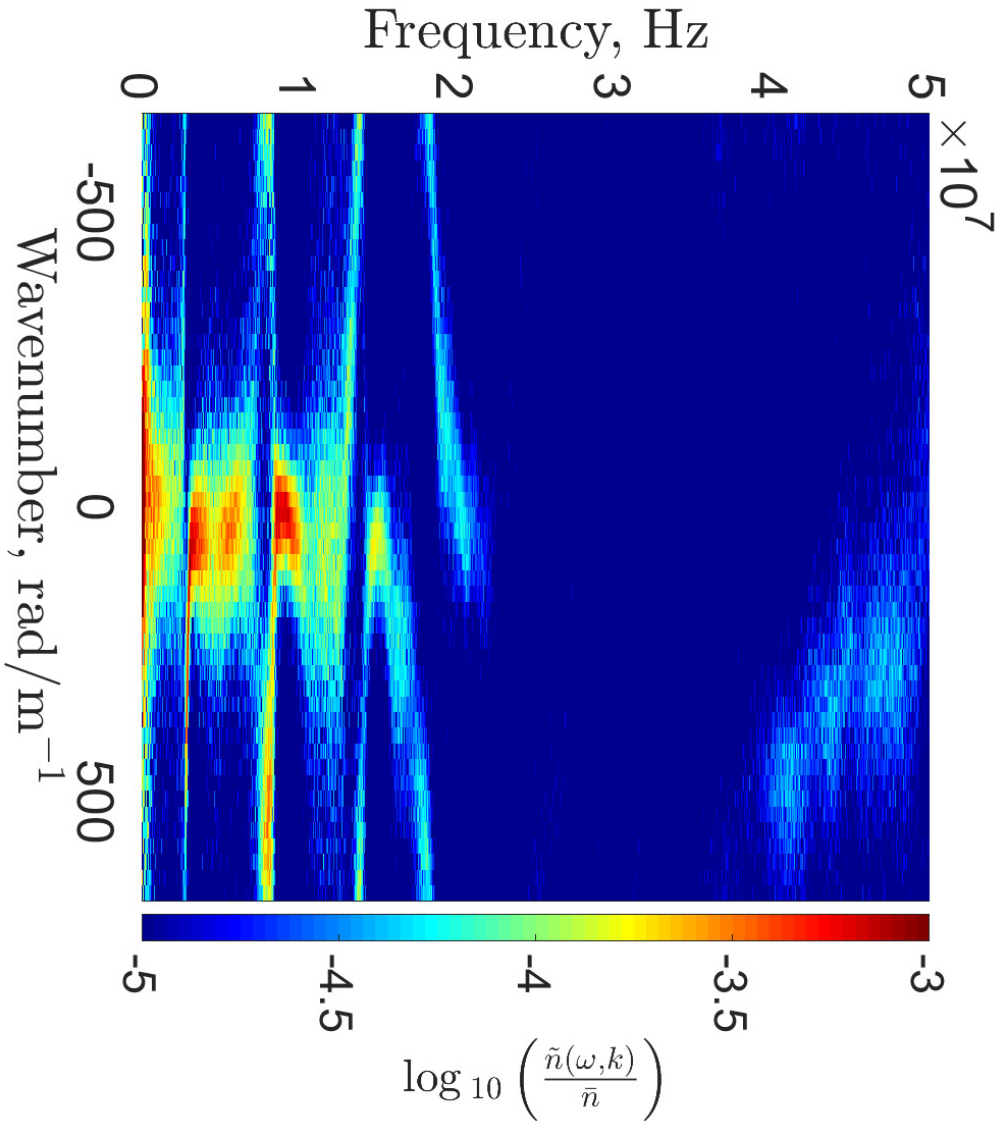

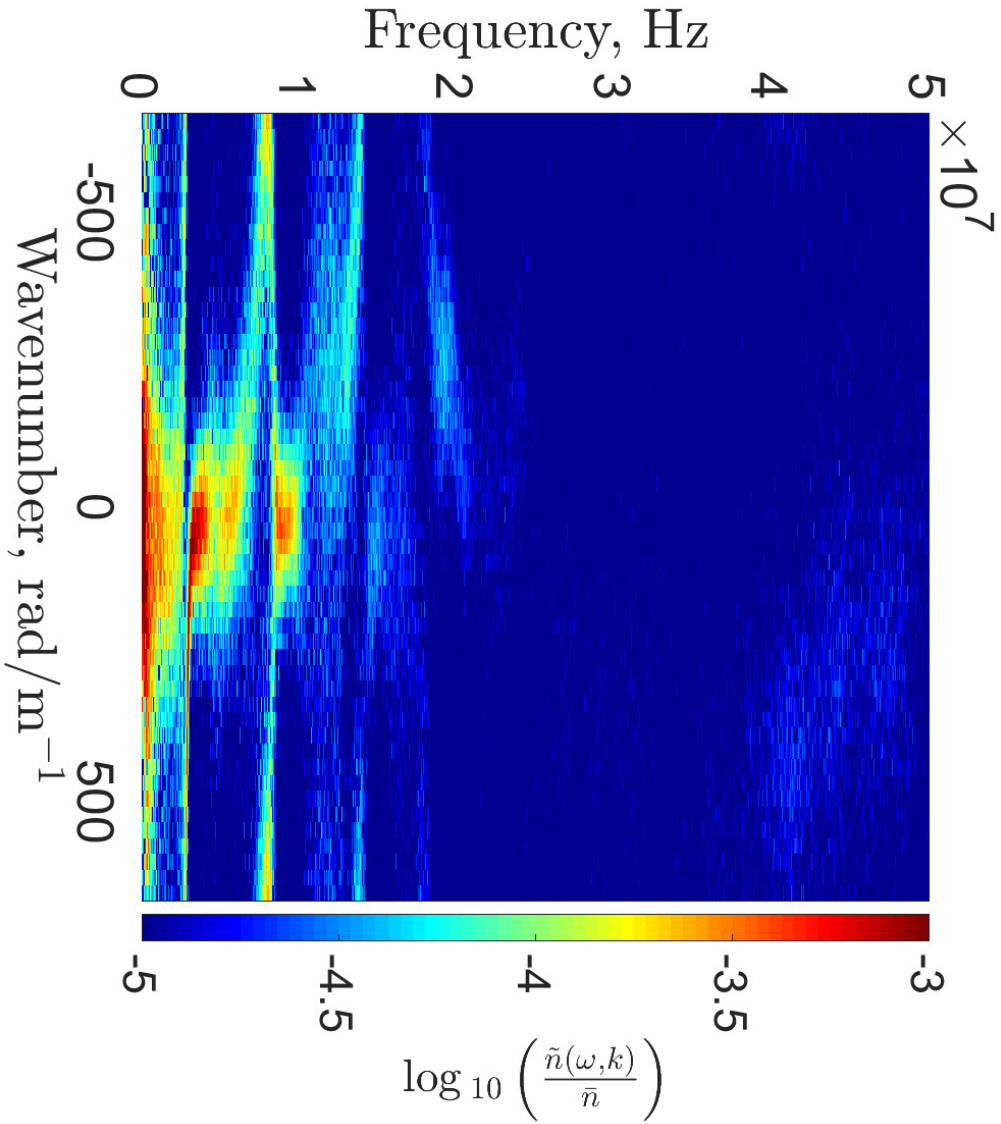

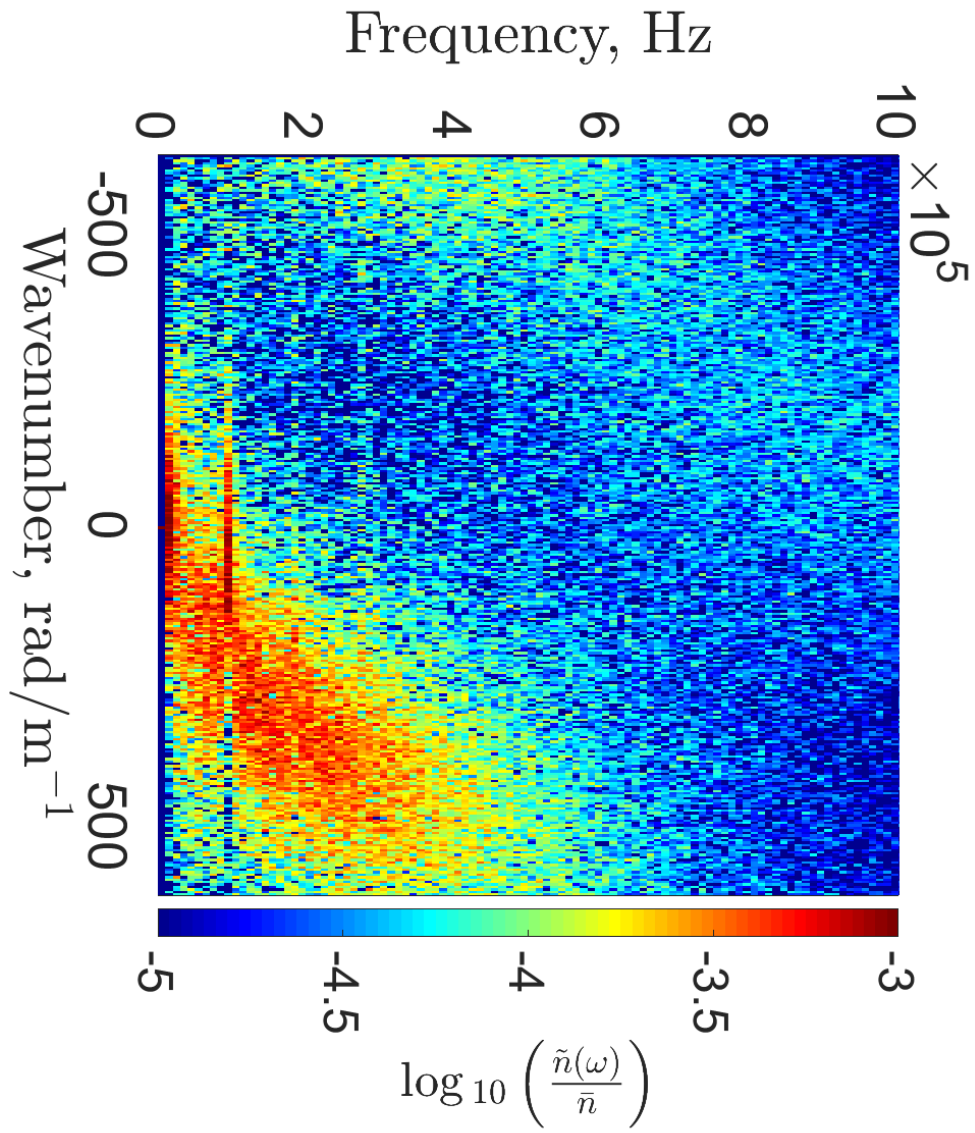

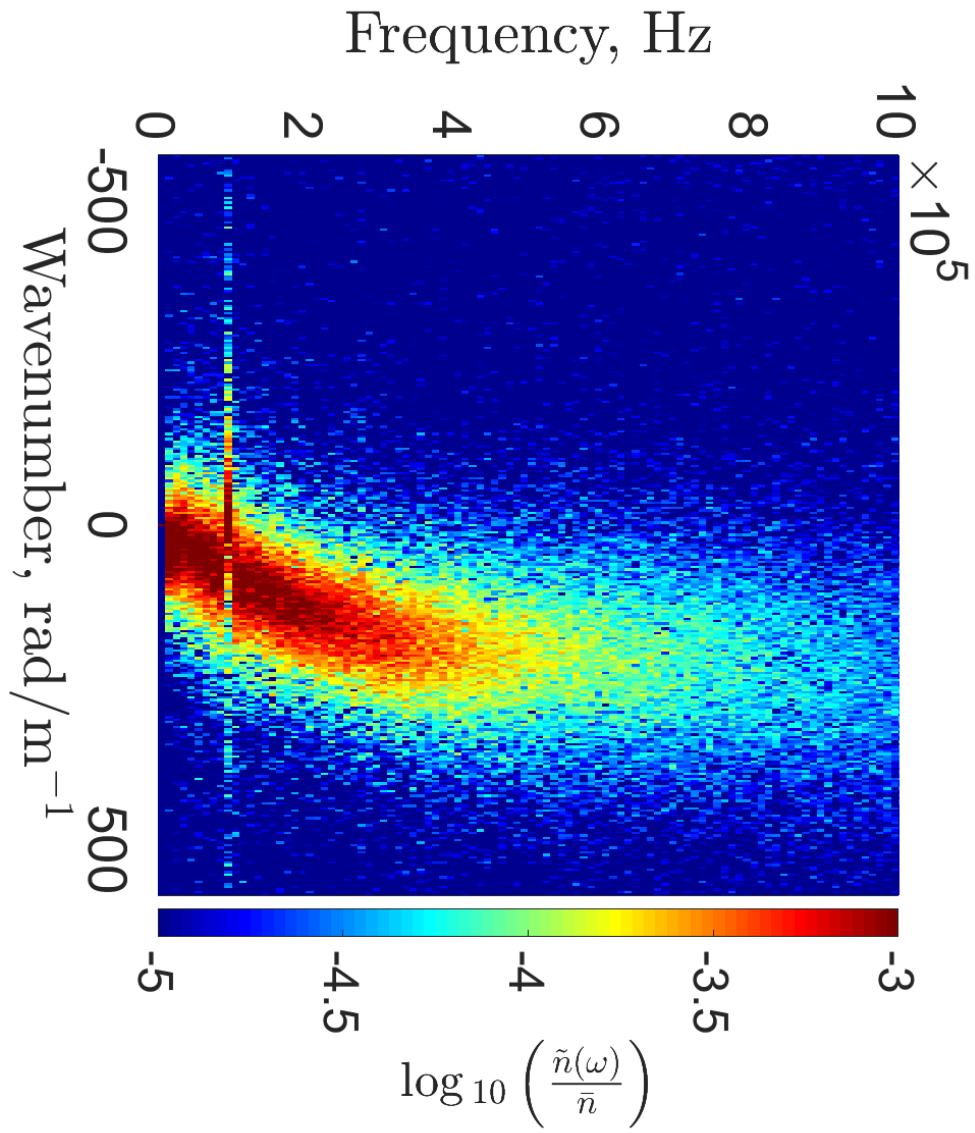

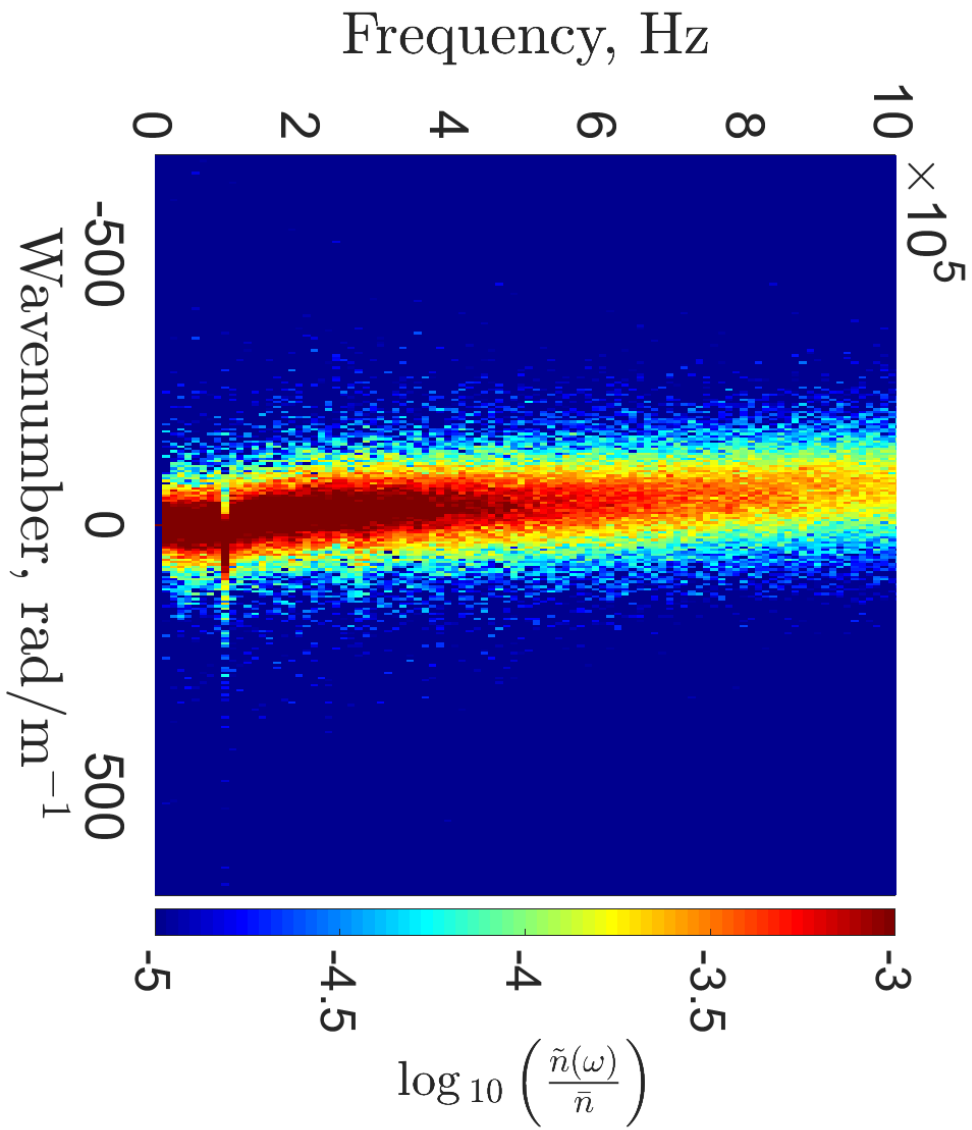

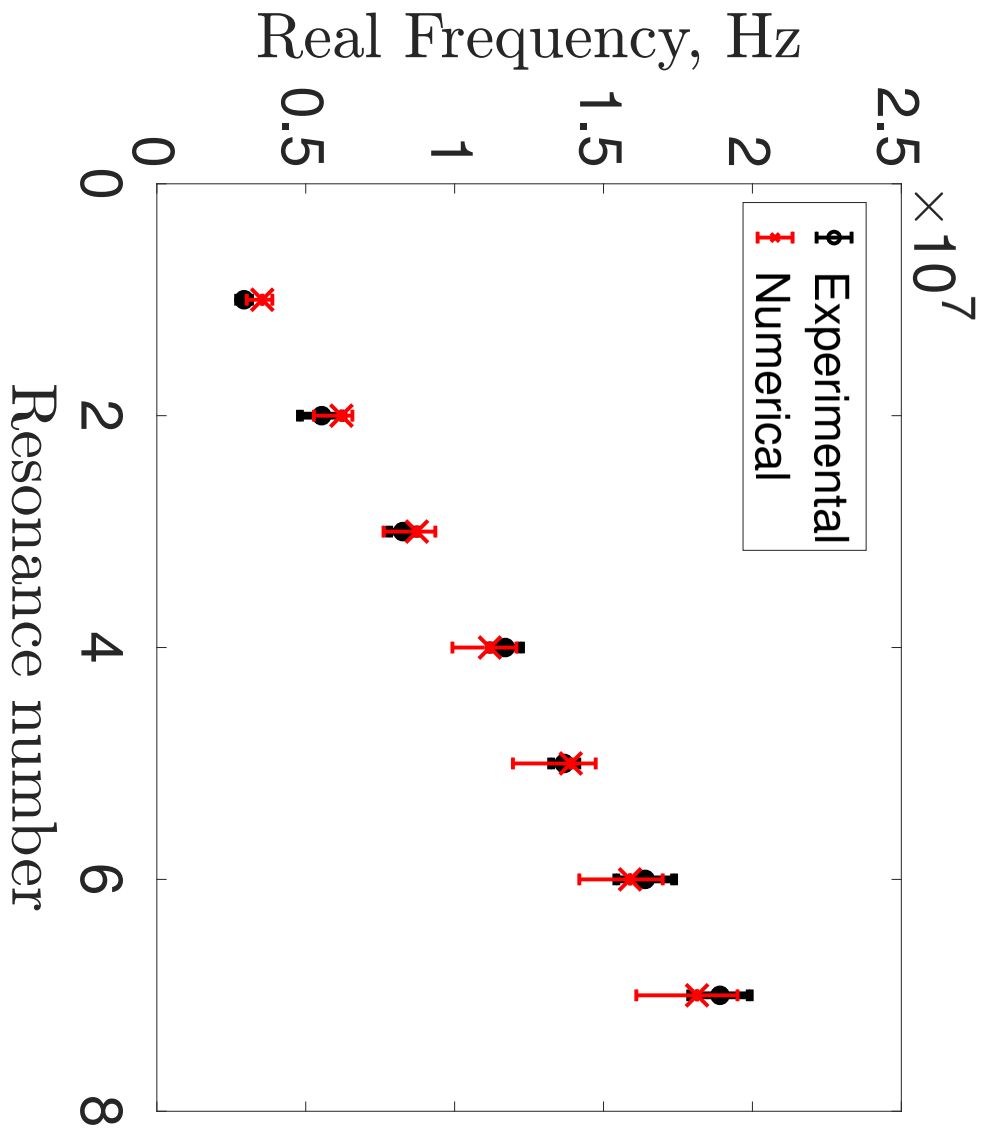

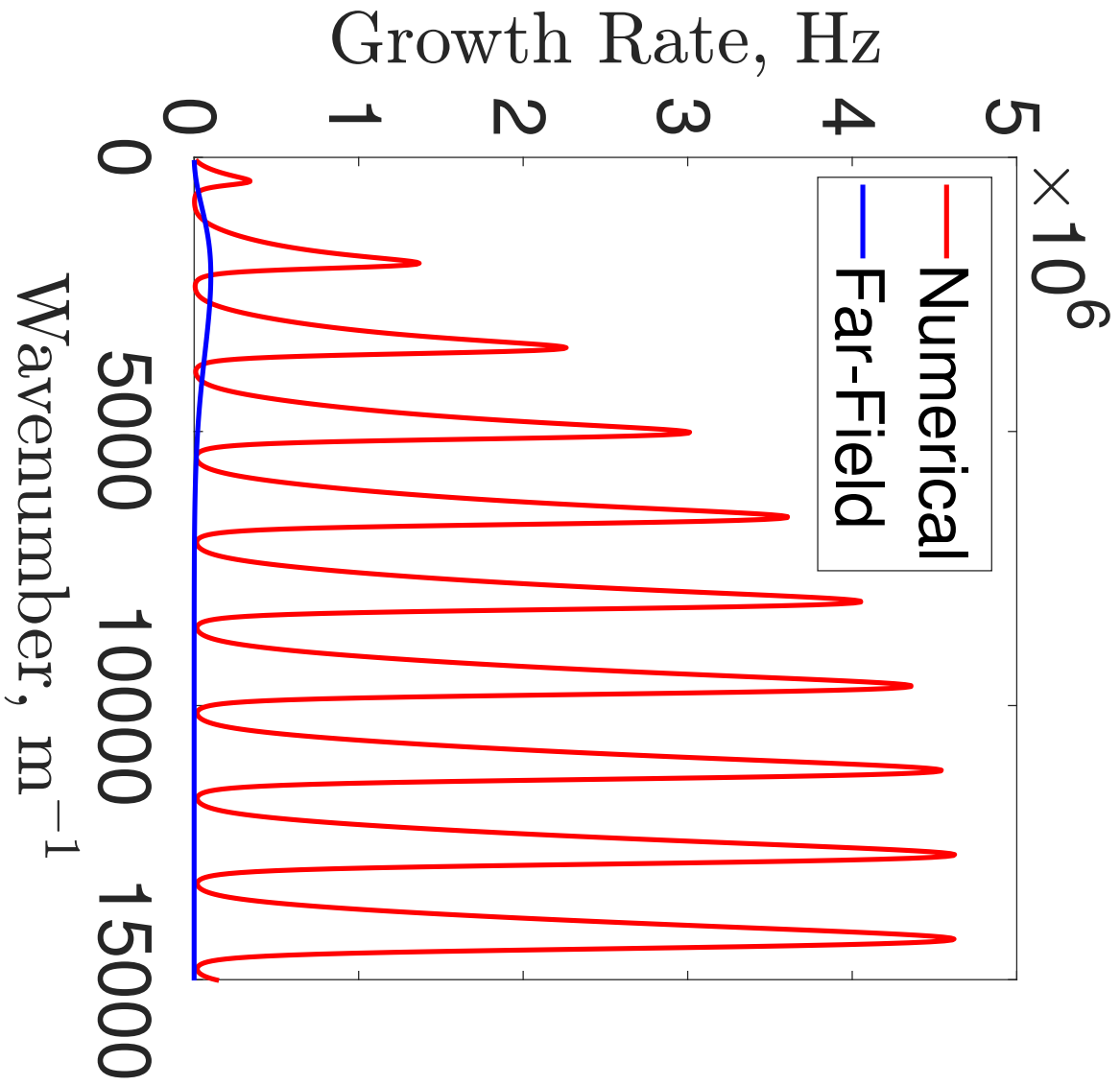

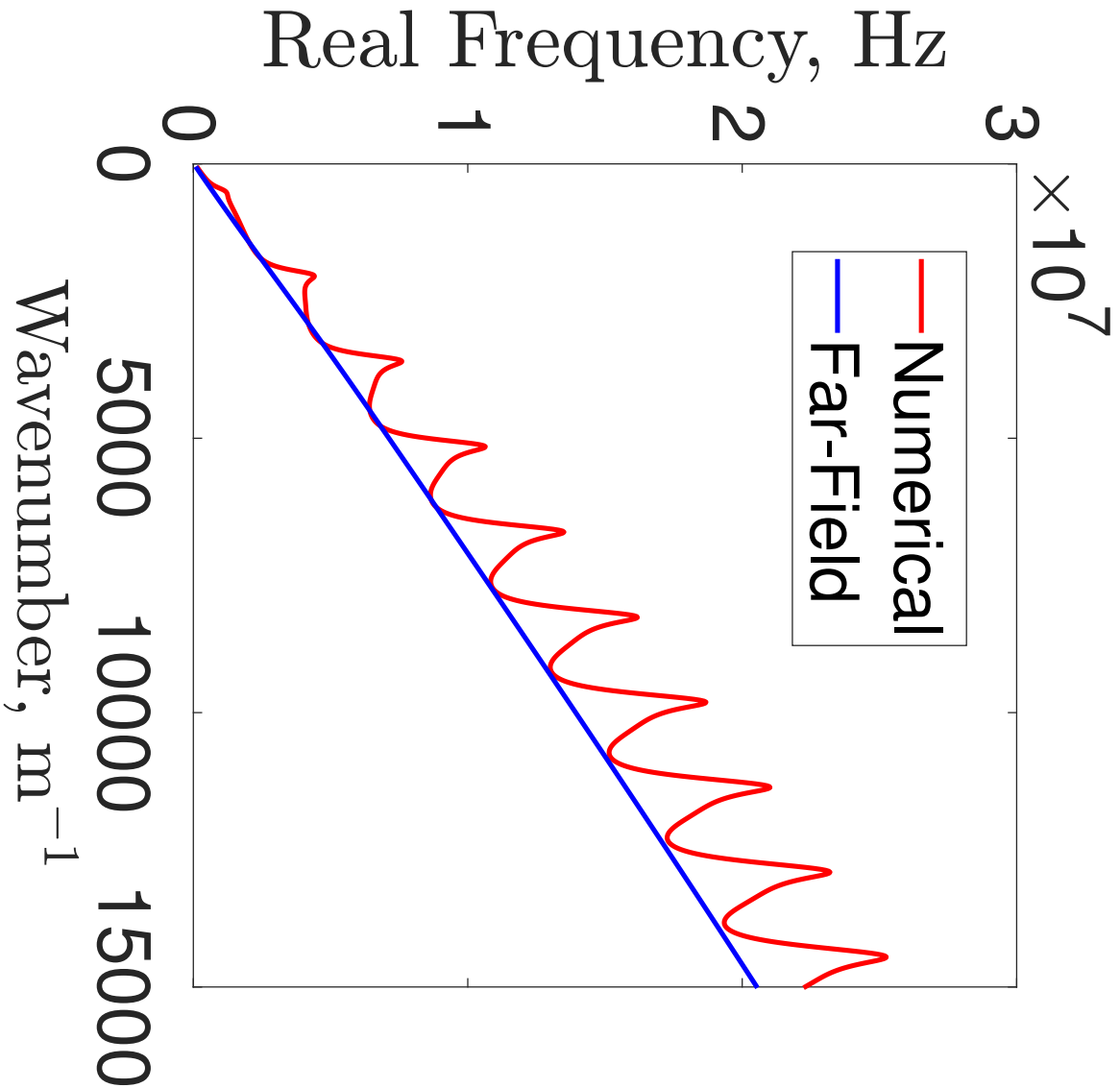

PLEASE CITE THIS ARTICLE AS DOI: 10.1063/1.5116708